LA-13430-T
Thesis

The Feed-Out Process: Rayleigh-Taylor and Richtmyer-Meshkov Instabilities in Thin, Laser-Driven Foils

Los Alamos
NATIONAL LABORATORY

Los Alamos National Laboratory is operated by the University of California for the United States Department of Energy under contract W-7405-ENG-36.

This thesis was accepted by the Department of Nuclear Engineering and Engineering Physics, University of Wisconsin-Madison, Madison, Wisconsin, in partial fulfillment of the requirements for the degree of Doctor of Philosophy. The text and illustrations are the independent work of the author and only the front matter has been edited by the CIC-1 Writing and Editing Staff to conform with Department of Energy and Los Alamos National Laboratory publication policies.

An Affirmative Action/Equal Opportunity Employer

LA-13430-T
Thesis

UC-712
Issued: April 1998

The Feed-Out Process: Rayleigh-Taylor and Richtmyer-Meshkov Instabilities in Thin, Laser-Driven Foils

D. Palmer Smitherman

Los Alamos
NATIONAL LABORATORY
Los Alamos, New Mexico 87545

Acknowledgments

Special thanks are extended to Dr. Glen Magelssen of Los Alamos National Laboratory (LANL) for his willingness to take on the responsibility of a graduate student. Gratitude is also extended to Nelson Hoffman of LANL for the many hours of educational discussions, and to the inertial fusion program at LANL for supporting this research. The Department of Energy funded my education through the Nuclear Engineering and Health Physics Fellowship, administered by the Oak Ridge Institute for Science and Education, for which I am indebted to them. The research described in this dissertation was financed by the Department of Energy under contract W-7405-ENG-36.

Table of Contents

List of Figures

Preface

This dissertation presents a computational and experimental study of feed-out, a hydrodynamic phenomenon that is important to inertial confinement fusion capsule implosions. The computational work was conducted at Los Alamos National Laboratory (LANL), in Los Alamos, New Mexico, with experiments performed at the NOVA laser facility located at the Lawrence Livermore National Laboratory in Livermore, California.

I was responsible for designing the experiments and the computational investigation of the phenomenon. Fielding the experiments was the responsibility of Robert Chrien, a staff scientist at LANL. I assisted Chrien during all but three of the shots, performing tasks such as metrologizing the targets, taking part in diagnostic alignment, and adjusting crystal angles in the spectrometers. Experimental questions involving code predictions, such as the X-ray camera timings, were decided by both Chrien and myself. Chrien analyzed the data and arranged for target fabrication, a service provided by the laboratory.

The first chapter of the dissertation provides an introduction to inertial fusion and an overview of the campaign. Chapter two is a review of relevant theories from the literature, while chapter three presents a more detailed account of the experimental procedure than found in chapter one. A discussion of computational considerations and the code used is found in chapter four.

Chapters two, three, and four are important. Science uses an iterative

process of theory and experiment to converge on the solution to a physical question. Theory provides physical understanding and may be used to predict the outcome of an experiment. Experiment is used to help confirm theoretical predictions. If the two answers disagree, it does not necessarily mean that theory is incorrect. Even if theory and experiment do agree, they could both be incorrect for different reasons. The rigor of the experimental and theoretical procedures is just as significant as agreement or disagreement between their respective results. When faced with a discrepancy between the two, the scientist must understand the limitations of each to resolve the problem. For example, could there have been a consistent machining error during target fabrication, or were the opacity tables used in the calculation less than optimal?

Computational and experimental results are discussed in chapter five. Details describing individual shots are found in the appendix including laser energies and diagnostic settings. The appendix also contains lessons learned while fielding the shots, such as which filter worked best with the X-ray cameras.

The terms "package," "foil," and "target" are frequently encountered in this work. "Package" and "foil" both refer to the planar slab of material placed on the side of the hohlraum, which was the subject of the hydrodynamic experiments. The target is collectively the package, hohlraum, backlighter, radiation shields, and alignment wire, all of which were placed in the laser target chamber and were the "target" at which the laser was fired.

DPS

THE FEED-OUT PROCESS: RAYLEIGH-TAYLOR AND RICHTMYER-MESHKOV INSTABILITIES IN THIN, LASER-DRIVEN FOILS

by

D. Palmer Smitherman

Abstract

Eight beams carrying a shaped pulse from the NOVA laser were focused into a hohlraum with a total energy of about 25 kJ. A planar foil was placed on the side of the hohlraum with perturbations facing *away* from the hohlraum. All perturbations were 4 μm in amplitude and 50 μm in wavelength. Three foils of pure aluminum were shot with thicknesses and pulse lengths respectively of 86 μm and 2.2 ns, 50 μm and 4.5 ns, and 35 μm with both 2.2 ns and 4.5 ns pulses. Two composite foils constructed respectively of 32 and 84 μm aluminum on the ablative side and 10 μm beryllium on the cold surface were also shot using the 2.2 ns pulse. X-ray framing cameras recorded perturbation growth using both face- and side-on radiography.

The LASNEX code was used to model the experiments. A shock wave interacted with the perturbation on the cold surface generating growth from a Richtmyer-Meshkov instability and a strong acoustic mode. The cold surface per-

turbation fed-out to the Rayleigh-Taylor unstable ablation surface, both by differential acceleration and interface coupling, where it grew. A density jump did not appear to have a large effect on feed-out from interface coupling. The Rayleigh-Taylor instability's vortex pairs overtook and reversed the direction of flow of the Richtmyer-Meshkov vortices, resulting in the foil moving from a sinuous to a bubble and spike configuration. The Rayleigh-Taylor instability may have acted as an ablative instability on the hot surface, and as a classical instability on the cold surface, on which grew second and third order harmonics.

1. Introduction

1.1 Inertial Confinement Fusion (ICF)

Inertial confinement fusion (ICF) is a process by which a small sphere of hydrogen, the capsule, is imploded using either a laser or particle beam [Duderstadt]. The hydrogen reacts to form nuclides with a lower total potential energy, releasing energy in the process. The hydrogen is usually a 1:1 mixture of deuterium and tritium (DT) because of the higher cross section of this reaction compared to other fusion reactions. The DT reaction is

$$D + T \rightarrow \alpha(3.5MeV) + n(14.1MeV).$$

Fusion cross sections are orders of magnitude smaller than their uranium fission counterparts, but reaction rates are proportional to the density of each ion species being burned and roughly scale to the fourth power of temperature. The ICF approach is to confine the capsule with its own inertia for a very short time, 100's of picoseconds, but produce extremely high reaction rates with high densities and temperatures on the orders of 10^3 - 10^4 times solid-state density and 10 keV respectively.

Historically, there have been three motivations for the study of ICF. They are commercial energy production, nuclear weapons physics, and pure scientific research. In the pursuit of each of these goals, ICF possesses advantages and disadvantages over the alternatives.

ICF offers the possibility of a more environmentally benign commercial

energy source than light water reactors or coal-fired plants. It would produce much less radioactive waste than conventional fission reactors, and no greenhouse gases. However, the storage of large amounts of tritium on site could represent an airborne radiation hazard to the local populace. ICF technology would have to advance greatly, at high initial investment, before an ICF power station could economically produce electricity.

The major competitor with fusion from a technical standpoint is a breeder reactor design with an accompanying waste transmutation reactor to destroy the long-lived daughter products and actinides. An equivalent alternative to the breeder-transmutation scheme would be designing a burner, which is a breeder that burns long-lived radioactive waste. Advanced breeders could be much safer and generate less long-lived radioactive waste than conventional reactors, but still more than ICF. The breeder would be much less expensive than ICF to develop, and have a high probability of success, as it represents a perturbation on presently operating technology. Present research focuses on DT fusion, but with the limited supply of lithium for tritium breeding, DT power might only represent a few centuries of electricity at current demand rates. If the more difficult DD fusion reaction could be harnessed, this achievement might represent thousands of years of power, but so could the breeder if uranium was mined from seawater. ICF for energy production would require a shift in the present research orientation from lasers to the more efficient ion beams, but even so, electricity from ICF looks doubtful.

With the present ban on nuclear weapons testing, ICF has taken on a more critical role in the understanding of weapons physics. Weapons science is often stated as a significant reason for building the National Ignition Facility (NIF), a 1.8 MJ ICF laser facility with which researchers hope to achieve ignition in ICF capsules. The NIF would be one of several facilities on which weapons physics experiments would be conducted. It appears significant that some of those designing weapons do not view the NIF and ignition as fundamental to weapons physics, and suggest that other experiments, which are more cost effective, should be considered in place of NIF. Another difficulty facing the NIF is that the exact purpose of ignition has not yet been clearly defined by the ICF community.

The last motivation for ICF research is pure science. Experiments can be designed to yield relevant data on astrophysical phenomena, such as instabilities in supernova. Equations of state in extreme regions of parameter space can be compared to theory and the interaction of strong radiation fields with matter investigated.

The most important machine for ICF research is the driver. The ICF driver provides the energy needed to compress the capsule and is usually a laser or particle beam. The driver may either directly interact with the capsule, as in direct drive, or with a metallic structure surrounding the capsule called a hohlraum, as in indirect drive [Hogan], see Figure 1-1. The hohlraum converts the incident driver radiation into X-rays, which illuminate the capsule and compress it.

Figure 1-1: Indirect and Direct Drive Inertial Fusion

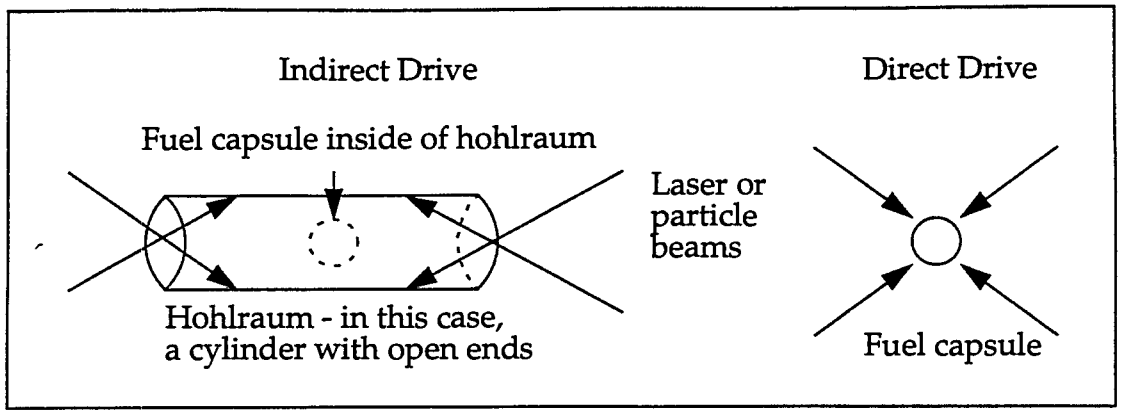

Hohlraums may be cylindrical, tetrahedral, or of many other shapes and are usually on order of one or two millimeters in size. Indirect drive produces a much more uniform radiation field with lesser laser beam quality than direct drive, thereby increasing capsule stability. The penalty is an energy loss in the conversion of laser energy to X-rays.

As ICF drivers, ion beams and lasers have different advantages [Hogan]. It is difficult to focus particle beams to the small size required to directly drive an inertial fusion capsule, unlike a laser driver. Lasers only have efficiencies of 0.25-8%, compared to the 20-30% for ion beams. Ion beams can also easily produce the megajoules of energy needed for ignition and burn, while it is difficult to produce this much energy with a laser. Everything considered, the Department of Energy's Fusion Policy Advisory Committee judged heavy-ion accelerators to be the leading candidate for a reactor driver. Currently, however, ICF research is using laser drivers because they are inexpensive compared to heavy ion facilities, and offer the potential to learn a great deal about capsule physics in the shortest

time. Some of this information would be transferable to an ICF ion facility.

The capsule is usually a sphere composed of two types of material, the hydrogen fuel on the inside, and an ablator on the outside. During the implosion, the pusher confines the fuel through inertia and converts the energy of the driver into mechanical work on the fuel. The pusher in this sense can be both the ablator as well as cold fuel adjacent to the ablator. The object is to first compress the capsule along a low adiabat to high density, then produce a small hot region at the center using converging shocks. The cold dense fuel adjacent to the "hot spot" traps alpha particles from the fusion process. In this way, the nuclear burn propagates through the capsule, and a much larger percentage of the energy needed to heat the capsule to fusion temperatures comes from fusion itself instead of the driver [Lindl].

The direct drive ICF capsule can be divided into three principal regions [Duderstadt] as shown in Figure 1-2. The most exterior is the energy deposition region, in which the laser light travels. The laser deposits energy here by inverse bremsstrahlung and resonance absorption, which is the coupling between electron plasma waves and light. Stimulated Raman scattering and stimulated Brillouin scattering are laser-plasma interactions that partially reflect the laser energy, and reduce absorption in this region. The limit of the energy deposition region is the critical density, where the plasma frequency becomes larger than the light frequency. Driver radiation does not penetrate past this point.

Figure 1-2: Direct Drive ICF Capsule

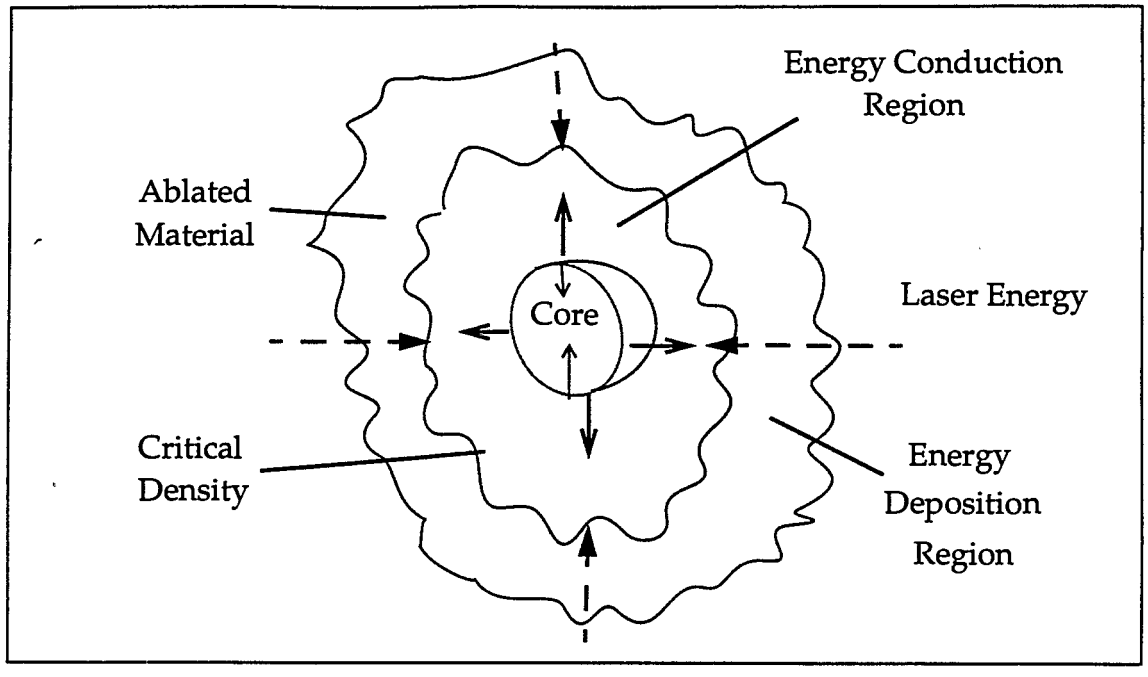

In the energy conduction region, material streams off the capsule surface and into the energy deposition region. Energy is transported by radiation and electron thermal conduction from the critical density to the ablation surface. Electron thermal conductivity is found to be much lower here than would normally be expected. The generation of large local magnetic fields and two-stream instabilities, generated from the heated electrons moving toward the capsule and the return current, can significantly reduce heat conduction by reducing the electron mobility.

The third region is composed of the core, or unablated DT material. By dividing the fuel disassembly time by the burn rate one finds the condition for a good burn in which a significant fraction of the fuel is consumed, tens of percent.

For a good burn, the integral of the fuel density along a radial line emanating from the center of the capsule to the pusher/fuel interface must be greater than 1 g/cm^2. Frequently this integral is termed "ρr." The range of a 3.5 MeV alpha is about 0.5 g/cm^2, so a ρr greater than 1 g/cm^3 also insures good fusion energy deposition in the fuel. It is not advantageous to continue to increase ρr without limit. It takes greater drive energy to compress to a higher ρr, but with diminishing returns in the fraction of fuel burned. An optimal value for DT fusion is about 3 g/cm^2, corresponding to roughly 30% fuel burn [Duderstadt].

For indirect drive, the physics of the laser interaction with the hohlraum is much the same as the energy conduction and absorption regions of a direct drive capsule. The hohlraum generates X-rays in the 100-200 eV range, which ablate the capsule, and interact directly with the surface throughout the implosion.

Of great importance to a successful implosion is symmetry. The hydrodynamics of an ICF capsule system is analogous to a basketball sitting on the point of a pencil. As long as the symmetry is perfect, the system is stable, but if there are any perturbations from this ideal state, the system quickly becomes unstable. Hydrodynamic instabilities cause any asymmetry on the capsule or in the DT to grow, resulting in mixing of the hot and cold areas of the fuel, mixing of the ablator and fuel, or complete disassembly of the capsule in extreme cases. In any event, much less of the fuel burns than if the implosion were perfectly symmetric. There are always perturbations from target fabrication on the surface of

the ablator and on the inside surface of the frozen fuel layer, see Figure 1-3. Present technology can limit these abnormalities to within a few micrometers in amplitude, but they are still a threat to proper implosion symmetry. Asymmetries in the radiation driving the capsule can create perturbations on the capsule surface by pushing harder on one region than another, in both indirect and direct drive. For example, if there is an imbalance in the power of the laser beams, the implosion will not be symmetric. For direct drive, the field intensities of the laser beams are variable in space and time, resulting in a "foot print" on the surface of the capsule early in time.

The two most important instabilities are the Rayleigh-Taylor and Richtmyer-Meshkov instabilities. After the drive pulse is turned on, the Rayleigh-Taylor instability, caused by a low density fluid pushing on a higher density fluid, results in growth of perturbations on the ablation surface. A shock wave begins to move through the capsule. When it reaches the inside surface of the DT ice, it interacts with the ice perturbations, generating a Richtmyer-Meshkov instability. As the ablator surface perturbations grow, they feed into the fuel, adding to the growth from the Richtmyer-Meshkov instability. When the shock arrives at the center of the capsule, it produces a low density, high temperature hot spot in the fuel. This light material begins to push outward on the converging colder material, eventually stagnating the compression. A Rayleigh-Taylor instability now develops during this deceleration phase on the interface between the hot and cold sections of the fuel, resulting in even greater internal perturbation growth. If the

Figure 1-3: Instability Time History in ICF Capsules.

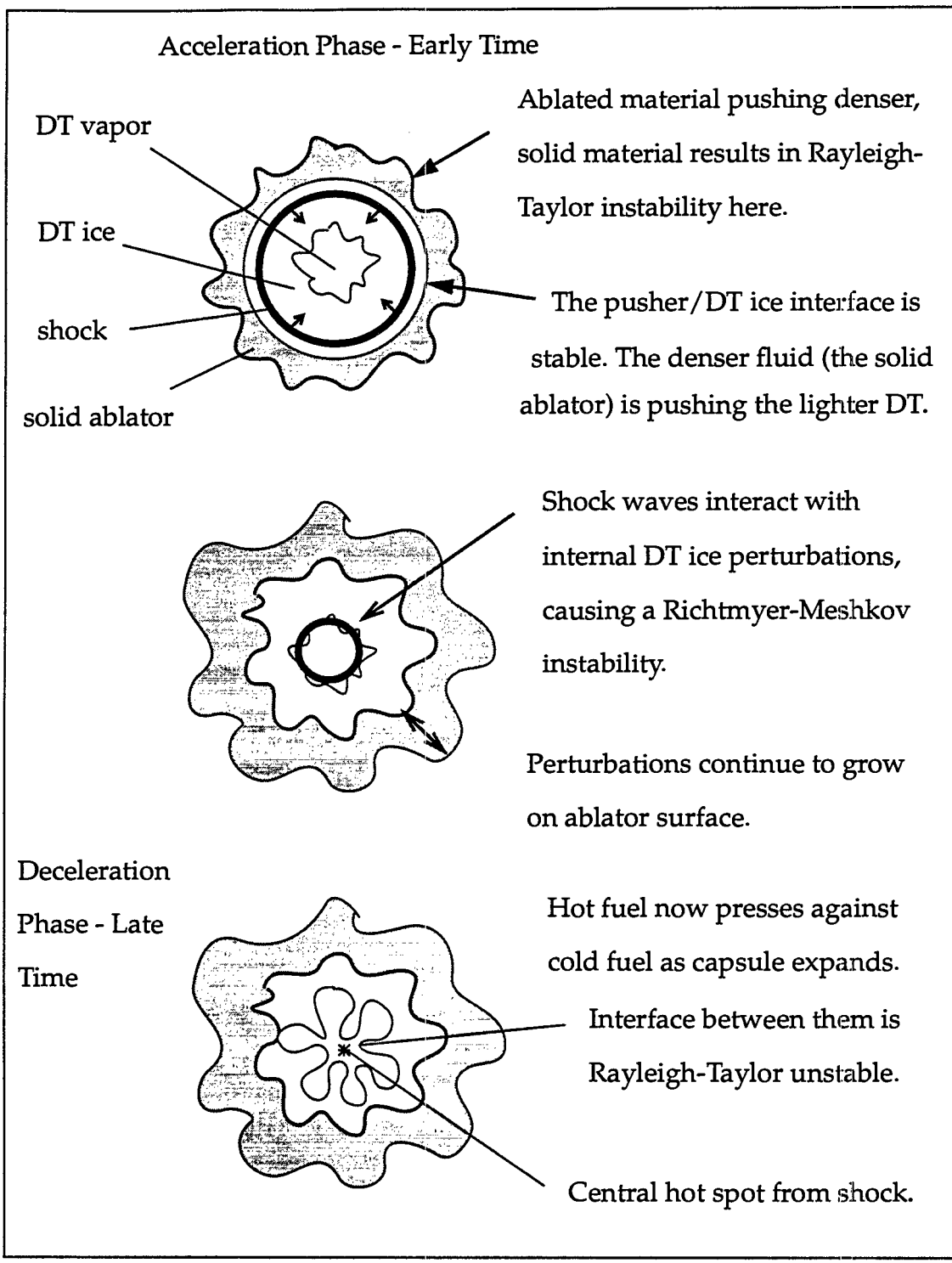

internal perturbations are too large, the hot spot cools and the capsule does not ignite. As of this writing, the ICF community has not yet achieved ignition in large part because of these reasons.

1.2 Purpose and Approach of Dissertation

To determine the effect ice perturbations of various amplitudes have on indirect drive NIF capsule performance, a robustness study was conducted by Hoffman and Wilson [Krauser] using the two-dimensional radiation-hydrodynamics code LASNEX, described in chapter 4. Hoffman calculated capsules with plastic ablators, while Wilson's capsules used beryllium. They both slowly increased the amplitude of the internal perturbations while giving the exterior perturbations and radiation drive perfect symmetry. As the amplitude increased, the neutron yields decreased.

The calculations showed a dramatic difference between the yield vs. roughness curves of the plastic and beryllium capsules. The plastic capsule fell to a zero yield at a roughness of 2 μm RMS, while the beryllium fell to a zero yield at a roughness greater than 8 μm RMS. The beryllium design was obviously much more resistant to perturbations on the ice than the plastic, but why?

Why beryllium was better was a difficult question to answer. Beryllium and plastic have different material properties and different equations of state. In addition, both materials were doped with high opacity elements. The shells were different masses. The plastic drive pulse was hotter than the beryllium pulse, but

the beryllium pulse was a little longer. At the end of the radiation pulse, the ablation front was closer to the DT in the plastic design than in the beryllium. To complicate matters further, Wilson assumed a Planckian drive spectrum for the beryllium capsule, while Hoffman included the high energy gold M-band in the spectrum for the plastic capsule calculations. The plastic capsule thus experienced greater preheat than the beryllium. Despite all of these differences, one important mechanism was suspected of creating the difference in the yield curves.

Sometime after perturbations begin to grow on the inside of the capsule, they also appeared on the outside of the capsule and begin to increase in amplitude. As they increased in amplitude on the ablation surface, they grew back into the capsule, eventually reaching the interior with an amplitude much larger than the original internal perturbations. The hydrodynamic communication of an interior perturbation to the exterior and its subsequent growth was dubbed "feed-out."

Figure 1-4 shows the sequence of events that occur in a planar slab during the feed-out process and is representative of what would occur in an ICF capsule with a smooth outer surface and perturbed interior. After the drive is turned on, the hohlraum radiation began to ablate the smooth side of the package, sending a shock wave through the material and compressing the package. A Richtmyer-Meshkov instability is created by the shock when it interacts with the perturbation on the back of the foil, causing the perturbations to phase-invert and grow. An acoustic mode is established behind the cold surface as part of the Rich-

tmyer-Meshkov flow field. A rarefaction wave, created by the reflection of the shock off the back side, began moving toward the ablation surface and is the leading edge of the Richtmyer-Meshkov flow field. After the rarefaction reaches the hot side, the ablation surface is "aware" of the perturbations on the back. A strong Rayleigh-Taylor instability located at the ablation surface then causes the pert-

Figure 1-4: Package Time Histories

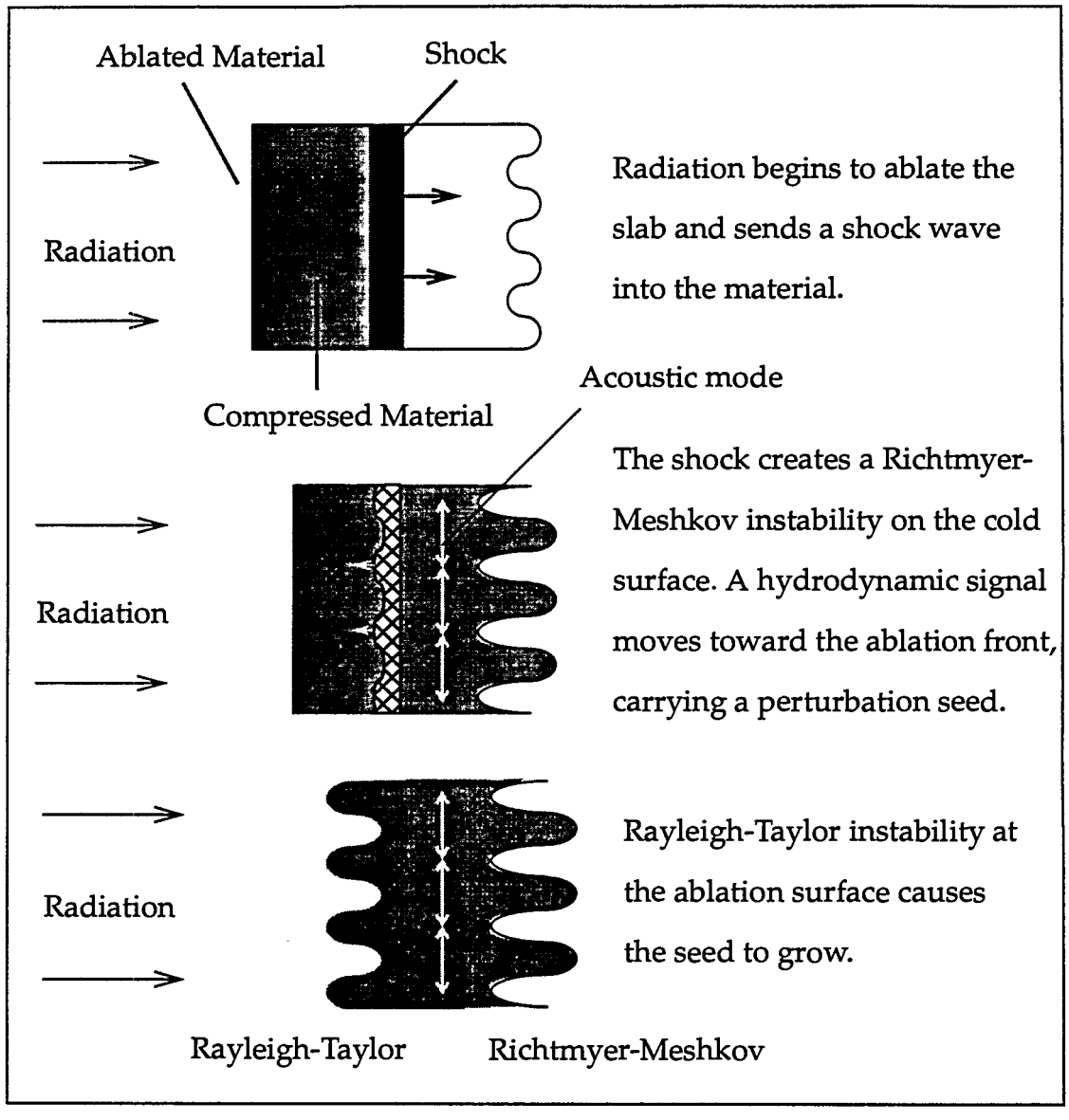

urbations on the hot side to grow. The Rayleigh-Taylor instability can only exist as long as the drive is on, but the Richtmyer-Meshkov instability is independent of the drive. As long as the foil is relatively thick, the Richtmyer-Meshkov and Rayleigh-Taylor instabilities grow independently. After radiation had burned through a significant amount of the foil, the two instabilities begin to interact. At this point, the perturbations on the ablation surface have fed-back through the foil and begin to perturb the cold surface.

At least two mechanisms are believed to seed the Rayleigh-Taylor instability on the ablation surface. The flow field of the Richtmyer-Meshkov instability on the cold surface could carry the perturbation back to the ablation surface. This mechanism is frequently referred to in this document as interface coupling. Alternately, perturbation growth on the surface could be seeded by a differential acceleration effect. There is less mass under the valleys of the initial perturbations than under the peaks. If the radiation drive was uniform, it would push the lower mass regions faster than the higher mass regions, resulting in a perturbation, and growth. Either or both could act as a seed for the Rayleigh-Taylor instability on the ablation surface.

Feed-out was immediately recognized as a serious threat to ICF capsules. The ablation surface is a highly unstable region. Perturbations grow rapidly on the ablation surface and can easily grow large enough to prevent the capsule from imploding properly. The exterior of the capsule may be polished to a roughness of about 10 nm RMS, but the interior of the DT ice perturbations cannot be

smoothed with present technology to less than about 0.5 μm RMS. During most of the time the capsule is imploding, the interior instabilities are not as severe as those on the ablation surface. One might conclude that the adverse effects of large internal perturbations would be mitigated by the short duration of the internal instabilities. The calculations of Wilson and Hoffman showed this may not to be the case. The larger internal perturbations coupled with the strong, long-duration ablation front instabilities during the implosion through feed-out, degrading the yield to unacceptable levels.

Differences in the feed-out of beryllium and plastic was suspected as the reason for the difference in the beryllium and plastic yield curves. Although the initial thicknesses of the beryllium and plastic ablators in the NIF capsule design were about the same, the beryllium ablated slower. As a result, the beryllium became thicker than the plastic in the implosion. The greater distance between the cold surface and the ablation front could have reduced the size of the Rayleigh-Taylor seed from feed-out in the beryllium. In addition, the greater distance could have also inhibited the Rayleigh-Taylor growth from feeding-back into the interior.

There was an additional important difference between the plastic and beryllium designs. The plastic had a density of about 1.0 g/cm^3, while the beryllium had a density around 1.85 g/cm^3. This meant that there was a much larger density jump at the intersection of the DT ice and the ablator in the beryllium than in the plastic. The ice had a density of 0.25 g/cm^3. Was it possible that a larger

density jump could be a greater barrier to interface coupling between the cold and hot surfaces? If the greater density jump was a barrier, the Rayleigh-Taylor seed from feed-out would have been smaller in beryllium than plastic.

In order to understand more clearly the reason for the superiority of beryllium over plastic, it was necessary to learn more about feed-out. Planar experiments were performed on the NOVA laser facility at Lawrence Livermore National Laboratory to experimentally confirm that feed-out exists and to study its dependence on thickness and density jump. Planar slabs of material very similar to the one displayed in Figure 1-4 were accelerated with radiation from a hohlraum. The slab is frequently referred to in this paper as the "package" or "foil." It was positioned in a small hole on the side of a hohlraum, so only the side facing inward, the hot side, received radiation, as shown in Figure 1-5. The hot side was smooth, while the side facing away from the hohlraum, the cold side, had a machined sinusoidal perturbation.

The two experimental setups used in the feed-out shots, face-on and side-on radiography, are shown in Figure 1-5.Notice the upper diagram displaying the face-on configuration. High energy X-rays were generated by firing two of NOVA's ten beams onto a small metal disk, the backlighter, on the opposite side of the hohlraum from the package. The specific energy of these X-rays was determined by the element comprising the backlighter but was always between 4.3 - 8.3 keV. There were holes in the hohlraum just large enough to allow passage of the X-rays through the hohlraum and through the package, after which they were

Figure 1-5: Experimental Setups for Face-on and Side-on Radiography

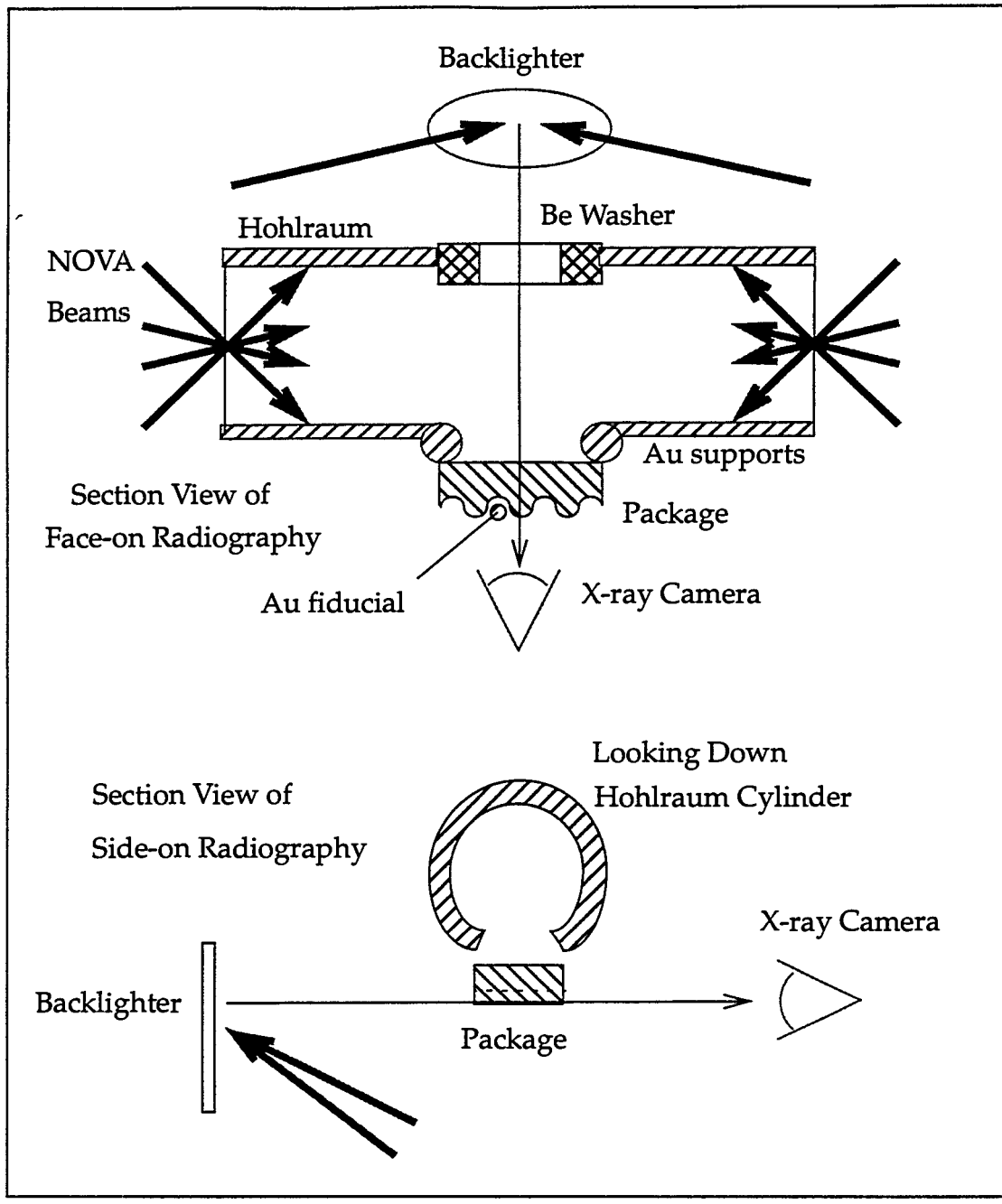

photographed with an X-ray camera. A beryllium washer was glued to the hole in the hohlraum on the backlighter side. Without the washer, gold vapor from the hohlraum would fill in the small hole. Gold was not transparent to the high energy X-rays from the backlighter, but beryllium was. A small gold wire was placed in the trough of the machined perturbations as a fiducial for phase changes. The line of sight of the camera was perpendicular to the plane of the package.

In face-on radiography, X-rays from the backlighter were attenuated more by passing through peaks in the perturbations of the package than by passing through the troughs. The difference in attenuation produced dark areas on the film from the valleys of the perturbations, and lighter areas from the perturbation peaks. The data could then be Fourier-analyzed to reveal the growth of the first, second, and third harmonics with time.

Face-on radiography quantitatively revealed perturbation growth, but did not show the location of the perturbations. They could be on the hot surface, the cold surface, or even in the center of the foil. Side-on radiography, also shown in Figure 1-5, revealed the location of the perturbations by placing the line of sight of the camera in the same plane as the package, and parallel to the initial perturbations. The backlighter likewise was repositioned to illuminate the package from the side. Package surfaces adjacent to and away from the hohlraum were thus simultaneously visible. Side-on radiography data was much more difficult to compare to calculations than face-on and only provided qualitative information.

In addition to the X-ray camera observing the package, two other diagnostics collected data on the backlighter to make certain it was performing as expected. One was an X-ray camera observing the side opposite laser irradiation. Low energy parts of the spectrum were filtered out passing through the disk, so only the higher energies used for the package diagnostic created an image. The purpose of this diagnostic was to ascertain when the backlighter was turned on and off, and how bright the source was qualitatively. A spectrometer connected to a streak camera observed the laser-illuminated surface, and showed the relative strengths of the high energy lines used for backlighting.

The X-ray drive was generated by focusing eight of NOVA's ten beams into the hohlraum. The hohlraums were constructed of gold due to its efficient conversion of the laser energy into X-rays. The M-band of gold always produced some 2-4 keV X-rays in addition to the thermal radiation. A total energy of 24 or 25.6 kJ in the hohlraum was requested on each shot, but in reality the energy varied from about 18-27 kJ.

Experimental design was a two-step process. First, a package with the desired characteristics was found by running various LASNEX simulations. A postprocessor, TDG, was then run to simulate data from the X-ray camera. The task for face-on radiography was to find the backlighter energy that would most effectively show the perturbations. For side-on radiography, an energy had to be selected that would show the density contours with the greatest perturbations. To some extent, these selections were based on trial and error. A detailed discussion

of backlighter selection for both face- and side-on geometries is presented in section 3.2.

In addition to designing the experiments, LASNEX was used to computationally study feed-out and to provide a better understanding of what was occurring in the shots. The computational results were compared to experimental data and conclusions drawn from both sets of results. The campaign was as much a computational as experimental effort.

For this initial investigation of feed-out, the desire was to observe experimental conditions ranging from weak to strong coupling of the ablation and cold surfaces. The level of coupling was adjusted by changing the thickness and pulse length, see Figures 1-6 and 1-7. Three cases were studied.

The first case was an 86 μm thick, aluminum foil. The thickness was large enough so that there was only weak coupling between the ablation and cold surfaces. The shock hit the rear surface of the "thick" package about the same time the drive was turning off, so only the Richtmyer-Meshkov instability was present. The thick package offered the opportunity to observe how the seed for the Rayleigh-Taylor developed.

The second foil had a thickness of 35 μm of aluminum. The shock from the drive pulse hit the rear surface of the "thin" package after about 1ns, at which time the drive had burned through much of the foil. The foil thickness was thus much less than the wavelength, resulting in strong and fast coupling of the Rayleigh-Taylor instability with the Richtmyer-Meshkov instability.

Figure 1-6: The 2.2 ns (PS-26) and 4.5 ns (PS-35) Laser Drive Pulses

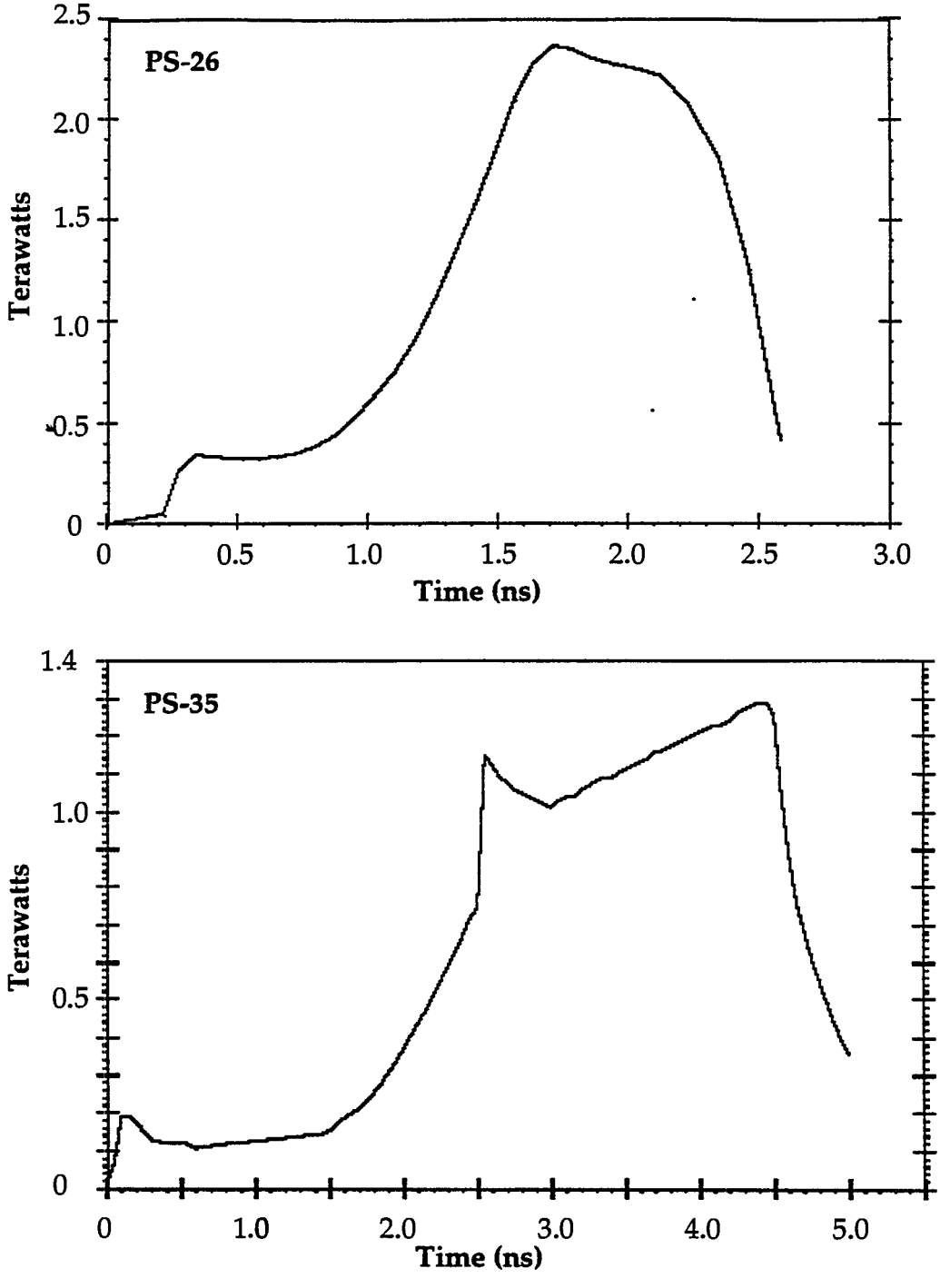

Figure 1-7: Packages That Were Shot

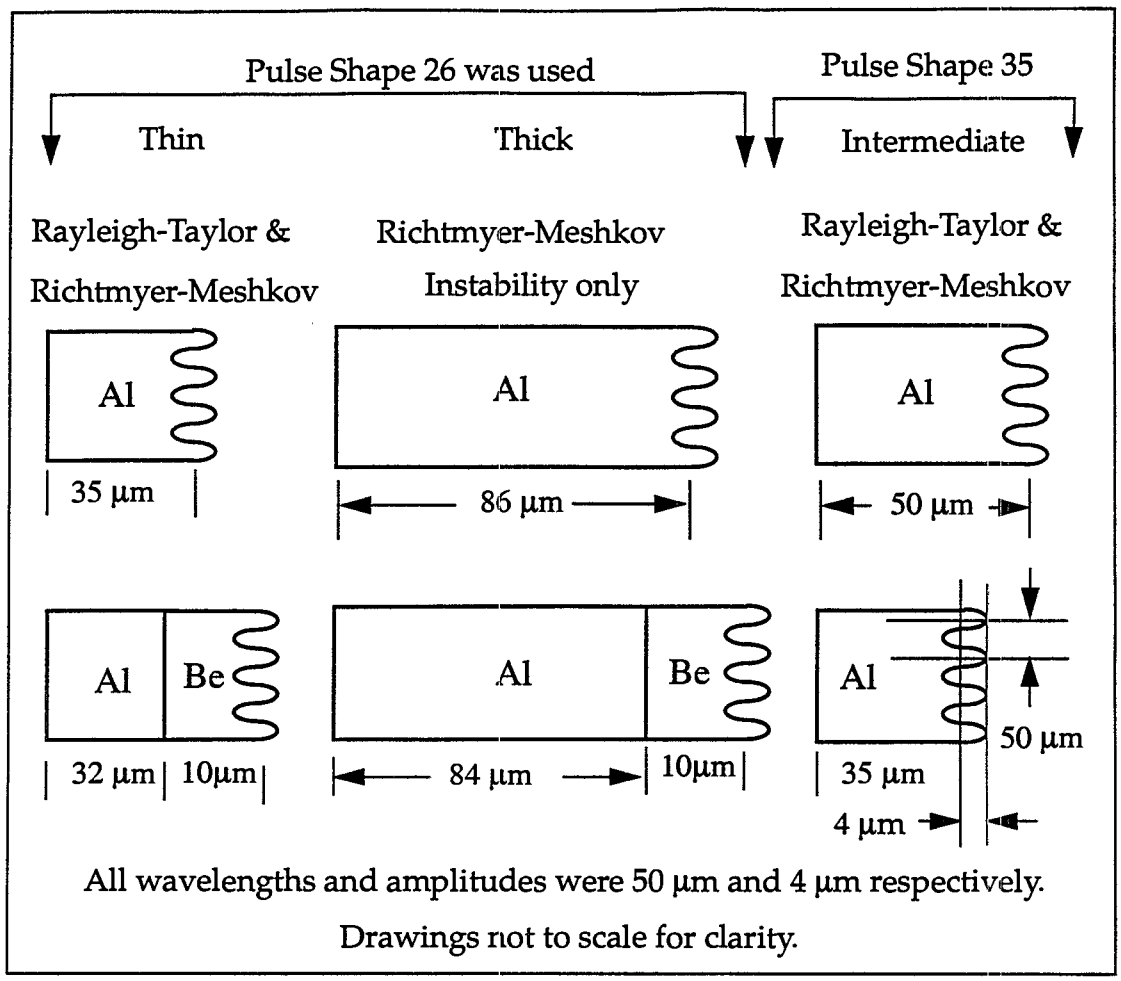

Both the thick and thin packages used a 2.2 ns long shaped pulse referred to as "PS-26," which produced a peak hohlraum temperature of 210 eV. A time dependent X-ray spectrum for PS-26 had previously been determined by calculation and experiment and was used in the feed-out calculations to drive the packages. The total energy of the spectrum could be increased or decreased in the calculation, but the spectrum as a function of time was fixed. The spectrum was non-Planckian and included contributions from the gold M-band emission.

In between the weak and strong coupling extremes was the most interesting situation, a foil that moved from independent Rayleigh-Taylor and Richtmyer-Meshkov instabilities to coupled instabilities as it burned through. The intermediate situation was closest to the NIF capsules.

The intermediate packages, which were 50 and 35 μm of aluminum, demonstrated a large amount of Rayleigh-Taylor growth. During the entire time the foils were moving from a decoupled to a coupled instability state, the Rayleigh-Taylor instability was causing the surface perturbations to grow. The intermediate case thus resulted in the greatest amount of Rayleigh-Taylor growth, and was easily designed by simply considering what factors would maximize the Rayleigh-Taylor growth. Package thicknesses were estimated by two competing factors. The package needed to be thick enough not to burn through before the pulse was over but as thin as possible in order for the Rayleigh-Taylor seed to reach the ablation front quickly. A long pulse was also needed to allow plenty of time for the instabilities to independently form, then to grow together as the foil burned through.

The pulse of choice for the intermediate packages was pulse shape 35, "PS-35," a 4.5 ns long pulse with a peak hohlraum temperature of about 160 eV. The PS-35 source used in the calculations was a time dependent Plankian obtained from experimental observation.

Beryllium was placed on the cold surface of some of the packages to study the effect a density jump would have on the feed-out. The density of beryl-

lium is 1.85 g/cm^3 compared to aluminum's 2.7 g/cm^3. An experimental benefit in using beryllium was its transparency to the backlighter. The initial perturbation in the beryllium could be observed growing into the aluminum ablator from the cold surface. Originally, each composite package was intended to be mass-matched to the pure aluminum package shown above it in the Figure 1-7. Mass-matching would have created similar accelerations and instability growth rates, making the two easier to compare. Due to fabrication errors, this was not exactly the case.

Aluminum was selected as the ablator material for several reasons. Ablator material in ICF capsules is always composed of low Z elements, usually with a Z less than 6. This is because atoms of a lower mass more efficiently convert the radiation into compressional energy. To better simulate the material of capsule ablators, it was desirable to use a low Z material in the feed-out shots. Unfortunately, low Z materials also have very low opacities and cannot effectively be observed with an X-ray camera. Aluminum was a good compromise as it is one of the lower Z elements whose opacity is suitable for X-ray backlighting. It also has a well-characterized equation of state, is easy to work with, and is readily available.

The initial perturbation on all packages had a 50 μm wavelength and 4 μm amplitude. The wavelength was selected to be approximately the same as package thickness, increasing the feed-out. The large initial amplitude introduced some nonlinear effects but was nevertheless desirable in order to insure that the

perturbations were diagnostically observable.

Experimental parameters varied slightly on each shot, and several shots were needed to obtain a good time history for each package. Some of these variations, such as drive energy, were recorded. Others, such as package thickness variations, could not be accurately ascertained.

After the experiments were completed, better calculations were pursued than those used in the design. Recorded experimental parameters from the shots and better opacities were included in later computational runs. Mathematica was used to Fourier-analyze the results and compare the time histories of the first, second, and third harmonics to experimental data. Zone size and radiation bin size were reduced until convergence was achieved in perturbation growth and radiation temperature respectively.

In summary, feed-out is an important effect in ICF physics because it couples the larger internal perturbations with the long-lived, strong ablation surface instabilities. Feed-out is believed to be partially responsible for the superiority of beryllium capsules designs to plastic capsule designs. In order to better understand the nature of feed-out, an experimental and computational campaign was undertaken to study the effects of a density jump and variations in the level of coupling between the cold and hot surfaces.

2. Theory

The physics of the feed-out packages may be understood with a system of coupled, nonlinear radiation-hydrodynamic equations, which will be discussed in this section. The radiation diffusion and Saha equations will be reviewed first, followed by a discussion on the equations of hydrodynamics. Special attention will be given to Rayleigh-Taylor and Richtmyer-Meshkov instability theories as aspects of the hydrodynamics.

2.1 Radiation

Radiation is an important aspect of the experiments presented in this paper. Radiation from the hohlraum ablates the feed-out foils and creates the shock wave which generates the Richtmyer-Meshkov instability. It preheats the packages and accounts for some of the heat transfer between different parts of the foils.

Radiation flow through the fluid is determined by the radiation transfer equation, which is a type of conservation equation. In Eulerian form, it may be written [Zel'dovich], as:

$$\frac{1}{c}\left(\frac{\partial I_\nu}{\partial t} + c\hat{\Omega} \bullet \nabla I_\nu\right) = j_\nu\left(1 + \frac{c^2}{2h\nu^3} I_\nu\right) - \kappa_\nu I_\nu, \qquad (1)$$

where c is the speed of light, h Planck's constant, and κ_ν and j_ν the absorption and emission coefficients for frequency ν respectively. The spectral radiant intensity is

I_ν. $I_\nu(\bar{r}, \overline{\Omega}, t)d\nu d\overline{\Omega}$ is the radiant energy in the spectral interval $d\nu$, passing per unit time, through a unit area, with the direction of energy propagation contained within the element of solid angle $d\overline{\Omega}$ about the vector $\overline{\Omega}$. The area is located at point $\bar{r}$ and is perpendicular to $\overline{\Omega}$. The second term on the left-hand-side of Eq. (1) is the rate at which radiation is leaving or entering the differential volume. Of the three terms on the right-hand-side, the first is spontaneous emission while the second is induced emission. Induced emission is emission caused by interaction of the radiation field with the material. The third is absorption.

Eq. (1) is a partial differential equation for radiation intensity as a function of position, time, and direction and describes a nonequilibrium radiation field. The effort required to solve Eq. (1) may be significantly reduced by assuming local thermodynamic equilibrium (LTE) and the diffusion approximation. LTE implies that the temperature of a sufficiently extended and optically thick material varies little over the mean free path of the photons, so one may assume the local distribution is Planckian instead of having to calculate it. From the viewpoint of a given test location, photons coming from a position with a different temperature and Planckian spectrum would be absorbed well before reaching the test point.

Radiation fields in LTE may be modeled with the diffusion approximation. The necessary condition for the existence of LTE, small temperature gradients in an extended, optically thick medium, serves simultaneously as justification for the use of diffusion theory because it forces the radiation intensity

into an almost isotropic state. If the radiation is anisotropic, then the diffusion approximation may not be used. Caution must be exercised in the application of diffusion to radiation, as the LTE assumption, isotropy, and therefore diffusion, may not be valid for all frequencies. For example, the peak of the hohlraum radiation spectrum used to drive the feed-out packages is about 150-200 eV. For most of the plasma, LTE at this temperature is a good assumption, but not for the ablated material. In addition, there are high energy components to the spectrum in the keV range. These photons stream through the packages with e-folding distances on the order of the size of the package, breaking the LTE assumption. As they represent only a small portion of the total energy in the radiation field, diffusion may still be used.

Diffusion in a radiation field in LTE may be written as:

$$\bar{S} = \int I_\nu \bar{\Omega}(d\bar{\Omega})d\nu = -\left(\frac{16}{3}\sigma l T^3\right)\nabla T, \qquad (2)$$

stating that the flux of radiant energy of all frequencies, $\bar{S}$, is proportional to the gradient of the temperature, T. The symbol l is the average mean free path for a Planckian distribution over all frequencies and is commonly termed the Rosseland mean free path. The total energy lost or gained per unit volume of fluid, per unit time due to radiation transport, q, is now simply $q = \nabla \bullet \bar{S}$. Thus, by assuming LTE and diffusion, the radiation transfer problem has been reduced to a problem very similar to heat transport. This approximation and is frequently known as the radiation heat conduction approximation [Duderstadt].

Some comments should be made in regard to the opacity of materials [Zel'dovich], μ, which is the sum of the scattering and absorption coefficients usually designated by κ's. Opacity is a strong function of the temperature of a material, because the opacity for the three forms of absorption, bound-bound, bound-free, and free-free, are so different. Bound-bound transitions correspond to the electron changing orbitals in the atom and have extremely large cross sections for very specific energies. Bound-free transitions can be from eight to eleven orders of magnitude lower in cross section than bound-bound, but represent a continuum of energies, unlike the bound-bound. A bound-free transition occurs when an electron is ejected from the atom. A free electron can only absorb energy from a photon if it is passing very close to an ion. If an ion is not in the vicinity, the electron can only serve as a scattering center for the photon. This type of absorption is referred to as free-free or inverse bremsstrahlung and has a cross section proportional to the square of the ion density. Of the three types of transitions, free-free tends to have the lowest cross section.

As temperature increases, the ionization increases, and so the opacity decreases. The density of ion states is thus very important for good opacities and is usually calculated with the Saha equation,

$$\frac{n_{m+1}}{n_m} = \frac{2}{n_e}\frac{u_{m+1}}{u_m}\left(\frac{2\pi m_e kT}{h^2}\right)^{3/2} \qquad u_m = \sum_{i=1}^{m} e^{-E_i/(kT)} .$$

The subscript m denotes the ionization state; n is the density of a particular state, n_e is the density of electrons, kT is temperature in units of energy, and E_i is the

excitation energy of the ion in the *i*th state; u is the partition function. The Saha equation is valid for local thermodynamic equilibrium.

From the above discussion, one can see the ablated material from the feed-out packages will be at a high temperature and have a low opacity and will be transparent to the hohlraum radiation. The ablation front will be composed of atoms in the process of being ionized and heated, and will absorb the bulk of the radiation from the hohlraum. Material behind the ablation front will have the highest opacity, and be the coldest. Only photons in the keV range will affect this region. Because of their long mean free path, the keV photons stream through the ablation front, depositing energy deep in the package. This results in expansion and preheat of the material before shock arrival, and may partially stabilize the Richtmyer-Meshkov instability by creating a density gradient.

2.2 Hydrodynamics

The physics of the feed-out experiments is dominated by hydrodynamics. The Rayleigh-Taylor and Richtmyer-Meshkov instabilities, which are the focus of these experiments, are hydrodynamic effects. The hydrodynamics controls the evolution of the perturbations, the density, velocity, pressure, and many other important fluid quantities.

The equations governing hydrodynamics are the equation of continuity, equation of motion, and the energy equation. The equation of continuity is derived by writing a mass balance over a volume of the fluid, and allowing the

volume to approach zero. Likewise, the equations of motion and energy are derived by writing balances over momentum and energy. A detailed derivation and description of these equations may be found in the text by Bird, Stewart and Lightfoot [Bird].

Some comments should be made as to why fluid theory is acceptable for the highly ionized gases that compose ICF packages. Both electromagnetic and hydrodynamic forces are present in these gases. There are two conditions necessary for the hydrodynamic forces to dominate. First, the ratio of the electromagnetic potential energy to the kinetic energy of a particle must be small. The potential energy comes from a test particle's interaction with other charged particles in the gas. As the particle moves through the fluid, a large kinetic energy and small electromagnetic potential energy results in small changes in velocity and momentum as it passes other charged particles. This effect is similar to what one would expect in a nonionized gas. The ratio of these two energies is easily calculated, as it is proportional to the inverse of the number of particles in a Debye sphere [Krall]. The second condition is that the frequency of collisions must be much greater than the plasma frequency. High collision frequency ensures that before the fields can effectively move a test particle any distance, collisions are pushing it in the direction of the flow.

There are two formulations of hydrodynamics. The Eulerian or conservative formulation is derived by writing the balance over a stationary volume element through which the fluid flows, and it represents the viewpoint of an

observer in the laboratory frame. In the Lagrangian formulation, the volume is flowing with the fluid, and the equations predict changes that occur as one follows a path with the fluid motion. These two methods are equivalent.

Eqs. (3)-(5) listed below are in Eulerian form. The variables are, ρ density, v velocity, t time, p pressure, g gravity, U internal energy, q heat flux, and ζ is the shear force per unit area due to viscosity. Velocity, heat flux and gravity are vectors, while ζ is a tensor. The equation of continuity is

$$\frac{\partial \rho}{\partial t} = -(\nabla \bullet \rho \bar{v}). \tag{3}$$

Rate of mass accumulation in differential volume at some point in the fluid.

Rate of mass flux in or out of differential volume.

The equation of motion is

$$\frac{\partial}{\partial t}\rho \bar{v} = -[\nabla \bullet \rho \bar{v}\bar{v}] \quad -\nabla p \tag{4}$$

Rate of increase of momentum per unit volume.

Rate of momentum gain by convection per unit volume.

Pressure force on element per unit volume.

$$-\nabla \bullet \underline{\zeta} \qquad + \rho \bar{g}.$$

Rate of momentum gain by viscous transfer per unit volume.

gravitational force on fluid element per unit volume.

The equation of energy is given by

$$\frac{\partial}{\partial t}\left(U+\frac{v^2}{2}\right) = -\left(\nabla\bullet\rho\bar{v}\left(U+\frac{v^2}{2}\right)\right) -(\nabla\bullet\bar{q}) \qquad (5)$$

Rate of gain of internal and kinetic energy per unit volume.	Rate of energy input per unit volume by convection.	Rate of energy input per unit volume by heat convection.
$+\rho(\bar{v}\bullet\bar{g})$	$-(\nabla\bullet\rho\bar{v})$	$-(\nabla\bullet[\underline{\zeta}\bullet\bar{v}])$.
Rate of work done on volume by gravity.	Rate of work done on fluid per unit volume by pressure forces.	Rate of work done on fluid per unit volume by viscous forces.

The Lagrangian formulation is written using a derivative following the fluid motion. This is called a substantial derivative, and is given by

$$\frac{D\psi}{Dt} = \frac{\partial\psi}{\partial t} + \bar{v}\bullet\nabla\psi = \frac{\partial\psi}{\partial t} + v_x\frac{\partial\psi}{\partial x} + v_y\frac{\partial\psi}{\partial y} + v_z\frac{\partial\psi}{\partial z}.$$

Applying this derivative to Eqs. (3)-(5) and using the continuity equation to simplify the results, the Lagrangian form is found to be

$$\begin{aligned}
\frac{D\rho}{Dt} &= -\rho(\nabla\bullet\bar{v}) \\
\rho\frac{D\bar{v}}{Dt} &= -\nabla p - [\nabla\bullet\underline{\zeta}] + \rho\bar{g} \qquad (6) \\
\rho\frac{D}{Dt}\left(U+\frac{v^2}{2}\right) &= -\nabla\bullet\bar{q} + \rho(\bar{v}\bullet\bar{g}) - (\nabla\bullet\rho\bar{v}) - (\nabla\bullet[\underline{\zeta}\bullet\bar{v}]).
\end{aligned}$$

Notice the equation of motion in Eqs. (6) is now in the form of Newton's second law, *mass x acceleration = force.*

There are three equations, not counting vectors, and four unknowns in the system of equations above, with the unknowns being $\bar{v}$, U, ρ, and p. The system needs to be closed with an equation of state, which is an equation relating one thermodynamic property to two others. In this case, there needs to be a relationship between U, ρ, and p. For an ideal gas, one may use $p = R\rho U$ where R is a constant of proportionality. Unfortunately, this is an overly simplified expression for ICF plasmas, which normally require the use of a tabulated equation of state from detailed calculations.

The hydrodynamic theories presented in the following sections often entail many assumptions in order to obtain simple, closed form solutions. The assumptions severely limit the practicality of the results, but they also allow for clearly understandable theories, providing great insight into the fundamental workings of the physics. Computational solutions are used to study the complete problems of radiation-hydrodynamics with fewer assumptions.

The following four sections focus on the Rayleigh-Taylor instability. A general overview of the Rayleigh-Taylor instability will be provided in section 2.2.1, then a derivation of the classical linear growth rate in section 2.2.2. A discussion on the effects of a density gradient and ablation will ensue. Section 2.2.3 is a review of mode coupling, while 2.2.4 discusses the effects of stratified fluids on the Rayleigh-Taylor instability. The Richtmyer-Meshkov instability will be presented in section 2.2.5 with a short discussion of mode coupling. The Richtmyer-Meshkov instability in stratified fluids is presented in section 2.2.6. Acoustic

modes, which are a result of the Richtmyer-Meshkov instability, will then be discussed in section 2.2.7. Section 2.2.8 presents a simple theory for feed-out from differential acceleration.

2.2.1 Introduction to the Rayleigh-Taylor Instability

The Rayleigh-Taylor instability occurs when the density and pressure gradients in a fluid have opposite signs, in other words, whenever a heavy fluid is accelerated by a lighter fluid. In this context, heavy and light refers to higher and lower density fluids respectively. A good example is when one turns a container of oil and water upside-down. The oil, which is a lighter fluid, is then supporting the water against acceleration from gravity. If the interface is perfectly flat, the system is stable, but if there are any perturbations on the interface, stability is lost and the perturbations begin to grow. The water moves to the bottom and the oil to the top. Entropy is thus increased by converting a state of ordered energy storage, potential energy of a top heavy fluid, to a state of disordered energy storage, turbulence and heat generated through viscosity.

Precisely how perturbations grow has been of intense interest to ICF researchers. Perturbation growth determines how capsule symmetry may be lost when different fluids begin to mix. The evolution of a single sinusoidal perturbation is particularly instructive in understanding the Rayleigh-Taylor instability, because any initial perturbation on the interface may be decomposed into a Fourier spectrum. The time history of a single mode is displayed in Figure 2-1. With

Figure 2-1: Time History of Rayleigh-Taylor Instability

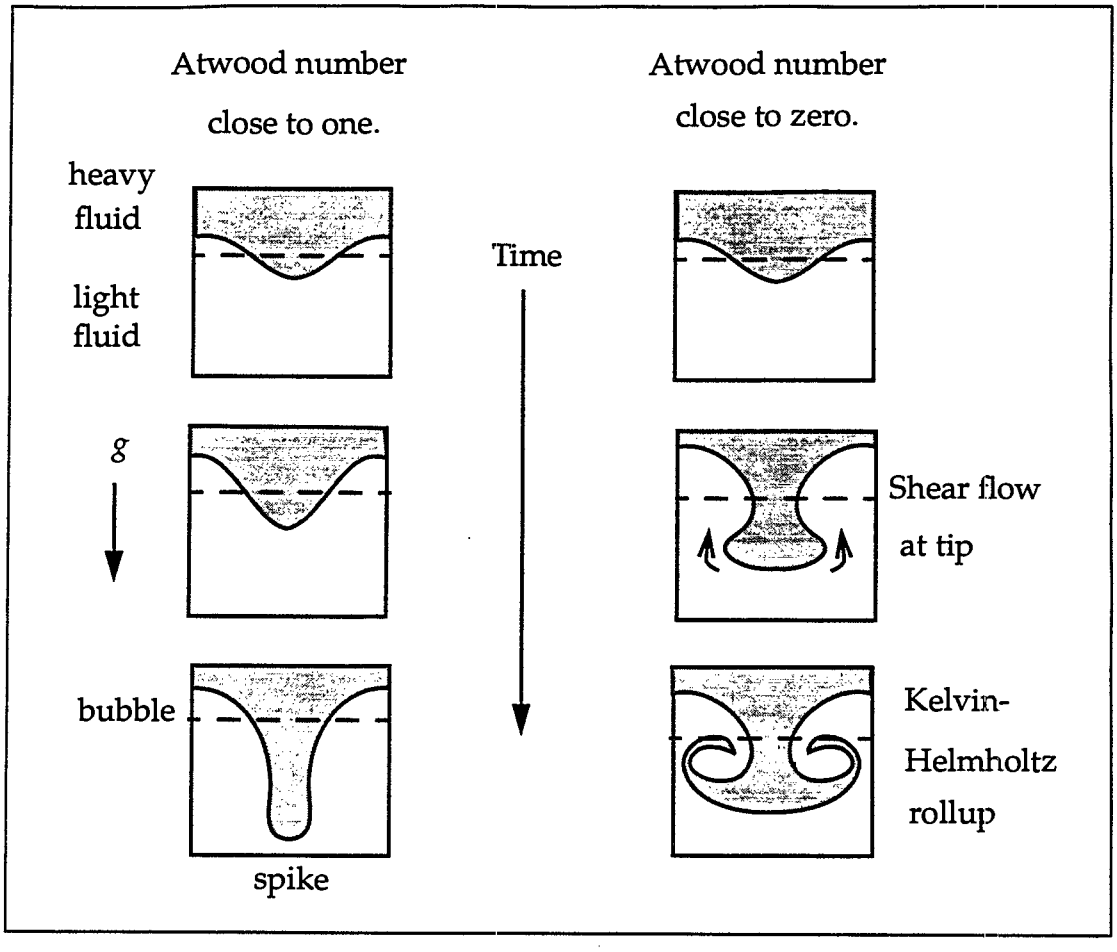

weak shocks and amplitudes less than a tenth the wavelength, the perturbation will grow exponentially early in time. Exponential growth may be derived by linearizing the hydrodynamic equations and is thus the linear phase of the instability. The time history of the perturbation amplitude, η, in this stage is given by

$$\frac{\eta(t)}{\eta_0} = e^{\gamma t} \qquad \gamma = \sqrt{gkA} \qquad k = \frac{2\pi}{\lambda},$$

where η_0 is the initial amplitude, k is the wavenumber, λ is the wavelength, and γ is the growth rate. The Atwood number, A, is defined as:

$$A = \frac{\rho_H - \rho_L}{\rho_H + \rho_L},$$

where ρ_H andρ_L are the densities of the heavy and light fluids respectively. The acceleration g is considered positive if it is directed from the heavy to light fluid. In that case, there is exponential growth of the perturbation. If the acceleration is directed from the light to the heavy fluid, then it is considered negative, meaning γ is imaginary. This results in stable oscillations, such as water waves.

When the amplitude is somewhere between a tenth to a whole wavelength, nonlinear effects become dominant and the growth slows down. At this point, the nature of the growth depends strongly on the Atwood number. For $A \cong 1$ the dominant effect is volume conservation of the high density fluid, with the constraint that the gravitational potential energy is minimized [Haan June 1991]. The light fluid flows upward into the heavy fluid in rounded shapes called bubbles, while the heavier fluid falls into the lighter fluid in long narrow spikes. The potential energy of the system is decreased by narrowing the spikes, with the tips moving further down.

The spike tips eventually reach free fall, while the bubbles rise at a constant velocity proportional to [Hoffman 1994]

$$v_B = \alpha\sqrt{\frac{2A}{1+A}g\lambda},$$

where α is a constant. This expression is the consequence of a balance between the buoyancy and drag forces acting on the bubble.

For $A \equiv 0$ as the spikes are being formed, they become altered by the Kelvin-Helmholtz rollup [Haan June 1991]. This is a shear instability that occurs at the interface of two fluids with different tangential velocities, see Figure 2-1. The linear growth rate for the Kelvin-Helmholtz instability is given by [Haan June 1991]

$$\gamma = k^2 v_R{}^2 \frac{\rho_1 \rho_2}{(\rho_1 + \rho_2)^2},$$

where ρ_1 and ρ_2 are densities of the two fluids and v_R is their relative velocity. As a spike pushes into the lighter fluid, there is a velocity differential between the tip of the spike and bottom of the bubble. The density term in γ for the Kelvin-Helmholtz instability is high, creating a fluid instability at the spike tips and retarding their growth. The result for small Atwood numbers is a symmetric mushroom between the light and heavy fluids. For intermediate Atwood numbers, one finds a spike with a mushroom on top. The feed-out packages have an Atwood number close to one, so the Kelvin-Helmholtz instability is not a concern.

Modeling of the Rayleigh-Taylor instability through its entire evolution requires different kinds of theoretical approaches. While $\eta < \lambda/10$, the linear theory is adequate. For the weakly nonlinear regime, potential flow models may be used, which assume the velocity may be described as a harmonic potential. Haan developed such a model, which will be described later [Haan August 1991]. It is valid only to second order, representing growth of the second harmonics. For the strongly nonlinear case with multiple interacting modes, a model was proposed

by Ofer [Ofer], improving slightly on one previously proposed by Haan [Haan June 1991, Hoffman 1994]. Ofer and his colleagues suggested using Haan's second order potential flow model up to the point where a mode begins to saturate, then switching over to a linear growth prescription more representative of saturation. The model is part analytical and part empirical. For very late times the Rayleigh-Taylor instability in the spike and bubbles phase, analytic theory may be used to predict very limited things such as the terminal bubble velocity. More commonly this regime is analyzed through computations and experiment and described by empirical formulas.

2.2.2 Single Mode Rayleigh-Taylor Growth

Following Hoffman [Hoffman 1994], the Rayleigh-Taylor instability growth of a single mode will be derived for a classical instability. The expression for the growth rate will then be amended by including terms to account for ablative stabilization, which is present in the feed-out experiments. The starting point is Eqs. (3) and (4), with the viscosity term removed from the momentum equation. By substitution of Eq. (3) into Eq. (4), one may obtain a simpler form of the momentum equation. The two equations together then are

$$\begin{aligned} \frac{\partial \rho}{\partial t} + \nabla\bullet(\rho\bar{v}) &= 0 \\ \rho\frac{\partial}{\partial t}(\bar{v}) + \rho(\bar{v}\bullet\nabla)\bar{v} &= -\nabla p + \rho\bar{g}. \end{aligned} \tag{7}$$

A small perturbation is introduced into the system by replacing each hydrody-

namic property in Eqs. (7) with two quantities, Eq. (8)

$$\begin{aligned} \rho &= \rho_0 + \rho_\pi \\ \bar{v} &= \bar{v}_0 + \bar{v}_\pi \\ p &= p_0 + p_\pi . \end{aligned} \tag{8}$$

The variables with the "0" subscripts represent equilibrium and are the "zeroth-order" aspect of the fluid motion. They satisfy Eqs. (7) by themselves, so one may write

$$\begin{aligned} \frac{\partial \rho_0}{\partial t} + \nabla\bullet(\rho_0 \bar{v}_0) &= 0 \\ \rho \frac{\partial \bar{v}_0}{\partial t} + \rho(\bar{v}_0 \bullet \nabla)\bar{v}_0 &= -\nabla p_0 + \rho_0 \bar{g} . \end{aligned} \tag{9}$$

The quantities with the subscript "π" in Eqs. (8) represent the perturbation being placed on the equilibrium properties and are very small. They are sometimes referred to as the "first-order" quantities.

After substituting Eqs. (8) into Eqs. (7), Eqs. (9) are subtracted, and the result is linearized. The process of linearization involves the elimination of any products of perturbed quantities, as these will be much smaller than terms that are linear in the first order terms. The linearized equations are

$$\begin{aligned} \frac{\partial \rho_\pi}{\partial t} + \nabla\bullet(\rho_\pi \bar{v}_0 + \rho_0 \bar{v}_\pi) &= 0 \\ \rho_\pi \frac{\partial \bar{v}_0}{\partial t} + \rho_0 \frac{\partial \bar{v}_\pi}{\partial t} + \rho(\bar{v}_\pi \bullet \nabla \bar{v}_0 + \bar{v}_0 \bullet \nabla \bar{v}_\pi) + \rho_\pi(\bar{v}_0 \bullet \nabla \bar{v}_0) &= -\nabla p + \rho_\pi \bar{g} . \end{aligned} \tag{10}$$

Now an initial condition is applied to Eqs. (10). For the Rayleigh-Taylor instability problem, one assumes the two fluids are initially at rest, implying,

$\bar{v}_0 = 0$. In addition, one can make a simplifying assumption that the flow is incompressible. Incompressibility is valid if accelerations in the flow are not strong enough to significantly change the density, and the fluid moves without either expanding or compressing. To apply this assumption, the divergence of the perturbed velocity is set to zero

$$\nabla \bullet \bar{v}_\pi = 0. \tag{11}$$

Substituting the initial velocity and incompressibility into Eqs. (10), one obtains

$$\begin{aligned} \frac{\partial \rho_\pi}{\partial t} + \bar{v}_\pi \bullet \nabla \rho_0 &= 0 \\ \rho_0 \frac{\partial \bar{v}_\pi}{\partial t} &= -\nabla p_\pi + \rho \bar{g}. \end{aligned} \tag{12}$$

For this derivation, it is assumed that gravity only acts in one direction, which is from the heavy to the light fluid, and perpendicular to the interface. Let this direction be $\bar{z}$, giving

$$g_x = g_y = 0. \tag{13}$$

In addition, ρ_0 is uniform throughout each of the fluids, with the exception of a discontinuity occurring at the interface. Thus, one may write

$$\frac{\partial \rho_0}{\partial x} = \frac{\partial \rho_0}{\partial y} = 0. \tag{14}$$

Because it is nonzero at the interface, the derivative of ρ_0 with respect to z must remain in the equations. Eqs. (13) and (14) are now substituted into Eqs. (12), with the result in component form below. Eq. (11) is also included because of

its usefulness.

$$\begin{aligned}
\rho_0 \frac{\partial v_{\pi x}}{\partial t} &= \frac{\partial p_\pi}{\partial x} & \frac{\partial \rho_\pi}{\partial t} + v_{\pi z}\frac{\partial \rho_0}{\partial z} &= 0 \\
\rho_0 \frac{\partial v_{\pi y}}{\partial t} &= \frac{\partial p_\pi}{\partial y} & \frac{\partial v_{\pi x}}{\partial x} + \frac{\partial v_{\pi y}}{\partial y} + \frac{\partial v_{\pi z}}{\partial z} &= 0. \qquad (15) \\
\rho_0 \frac{\partial v_{\pi z}}{\partial t} &= \frac{\partial p_\pi}{\partial z} - \rho_\pi g
\end{aligned}$$

Eqs. (15) are solved by Fourier transforming, which converts the derivatives into products. Only transformations with respect to x and y, are made, as the z direction does not share the same symmetry as the other two directions. The following Fourier transform pairs are defined:

$$\begin{aligned}
V_{\pi x}(k_x, k_y, z, t) &\leftrightarrow v_{\pi x}(x, y, z, t) & P_\pi(k_x, k_y, z, t) &\leftrightarrow p_\pi(x, y, z, t) \\
V_{\pi y}(k_x, k_y, z, t) &\leftrightarrow v_{\pi y}(x, y, z, t) & R_\pi(k_x, k_y, z, t) &\leftrightarrow \rho_\pi(x, y, z, t). \\
V_{\pi z}(k_x, k_y, z, t) &\leftrightarrow v_{\pi z}(x, y, z, t)
\end{aligned}$$

The zeroth-order quantities are not functions of x and y, which simplifies the Fourier transforms. k_x and k_y are the x and y components of the wavevector, $\bar{k}$, with a magnitude of $k = \sqrt{k_x^2 + k_y^2}$, which is called the wavenumber. The wavelength that corresponds to a particular wavenumber is given by, $\lambda = (2\pi)/k$. In solving Eqs. (15), one may assume the time dependence of the solution is proportional to $e^{i\gamma t}$, which is a standard assumption for finding solutions with the Fourier transform. After performing the transforms and substituting the time dependence, Eqs. (15) become

$$\begin{aligned} \gamma\rho_0 V_{\pi x} &= -ik_x P_{\pi x} & \gamma R_\pi + V_{\pi z}\frac{\partial \rho_0}{\partial z} &= 0 \\ \gamma\rho_0 V_{\pi y} &= -ik_y P_{\pi y} & ik_x V_{\pi x} + ik_y V_{\pi y} + \frac{\partial V_{\pi z}}{\partial z} &= 0. \\ \gamma\rho_0 V_{\pi z} &= -\frac{\partial P_\pi}{\partial z} - R_\pi g \end{aligned} \tag{16}$$

After some algebraic manipulations of Eqs. (16) and with the help of the definition of the wavenumber, one may write

$$\frac{\partial}{\partial z}\left(\rho_0 \frac{\partial V_{\pi z}}{\partial z}\right) = k^2 \rho_0 V_{\pi z}\left(1 - \frac{g}{\gamma^2 \rho_0}\frac{\partial \rho_0}{\partial z}\right). \tag{17}$$

Eq. (17) is an eigenvalue problem, meaning it only has solutions for a specific pair of γ and $V_{\pi z}$, once k, g, and $\rho_0(z)$ have been defined; γ is the eigenvalue, while $V_{\pi z}$, is an eigenfunction.

Away from the interface, ρ_0 is constant, so its derivatives are zero. One may thus cancel it from Eq. (17) and remove the derivatives. This leaves

$$\frac{\partial^2 V_{\pi z}}{\partial z^2} = k^2 V_{\pi z},$$

which has the general solution,

$$V_{\pi z} = A(k_x, k_y, t)e^{kz} + B(k_x, k_y, t)e^{-kz}.$$

The vertical velocity should vanish at infinity, implying $B = 0$ for $z < 0$ and $A = 0$ for $z > 0$. The two solutions should match at the interface, where at time zero there is some initial condition, $X(k_x, k_y) = V_{\pi z}(k_x, k_y, z = 0, t = 0)$. The solu-

tion should also contain an exponential time dependence, as this was the basis for the derivation of Eqs. (16), resulting in the solution

$$V_{\pi z} = \left\{ \begin{array}{l} X(k_x, k_y)e^{kz}e^{\gamma t}, z < 0 \\ X(k_x, k_y)e^{-kz}e^{\gamma t}, z > 0 \end{array} \right\}.$$

To calculate γ, an additional boundary condition is needed. By integrating Eq. (17) over the interface along an infinitesimally small element of the z axis, a jump condition may be obtained

$$\lim_{\varepsilon \to 0} \int_{-\varepsilon}^{+\varepsilon} \left(\frac{\partial}{\partial z}\left(\rho_0 \frac{\partial V_{\pi z}}{\partial z} \right) - k^2 \rho_0 V_{\pi z}\left(1 - \frac{g}{\gamma^2} \frac{\partial \rho_0}{\partial z} \right) \right) dz = 0$$
$$-kW(\rho_H + \rho_L) + \frac{k^2 g}{\gamma^2} W(\rho_H - \rho_L) = 0. \qquad (18)$$

Solving for γ,

$$\gamma^2 = kg\frac{(\rho_H - \rho_L)}{(\rho_H + \rho_L)} = kgA. \qquad (19)$$

Eq. (19) shows the origin of the Atwood number, A. Notice there is a positive and negative component of the square root, yielding growing and decaying modes.

At least two other factors add stability to radiation-ablated plasmas that are not accounted for in Eq. (19), a density gradient and the ablation process itself. In the feed-out experiments, ablation partially stabilizes the instabilities on the hot surface, while a density gradient partially stabilizes instabilities on both surfaces. Density gradient stabilization will be presented first.

Consider a more realistic ICF situation including radiation from either a hohlraum or a laser. As radiation ablates material from a solid foil, the ablated material streams away into vacuum, and a flat density gradient is formed. The growth of a perturbation on this gradient is an eigenvalue problem like the growth on a sharp interface, with the specific eigenvalue and eigenfunction depending on the density profile. For an exponential density profile, the eigenfunction is exponential, as in the sharp interface problem. The eigenvalue cannot be written down in closed form, although one may approximate it.

A back of the envelope estimate is possible by deriving an effective Atwood number [Haan June 1991]. In the sharp interface situation, the perturbation falls off away from the interface as $e^{-k|z|}$, thus sampling effective densities at $z = \pm 1/k$. Assuming the density varies as $e^{z/L}$, where L is some scale length, then the effective densities of the perturbation samples are

$$\rho_H = \rho_0 e^{1/(kL)} \qquad \rho_L = \rho_0 e^{-1/(kL)}.$$

Giving an effective Atwood number and growth rate of

$$\begin{aligned} A &= \frac{\rho_H - \rho_L}{\rho_H + \rho_L} = \tanh\left(\frac{1}{kL}\right) \\ \gamma &= \sqrt{gk\tanh\left(\frac{1}{kL}\right)}. \end{aligned} \tag{20}$$

For $kL \gg 1$, the perturbation wavelength is much smaller than the density scale length, resulting in an effective Atwood number close to zero. This represents the maximum stabilizing effect of the gradient, with the growth rate

approaching $\gamma \rightarrow \sqrt{g/L}$. For $kL \ll 1$, the perturbation is much bigger than the density scale length. The effective Atwood number approaches one, with the growth rate becoming, $\gamma \rightarrow \sqrt{gk}$. Stabilization of the interface thus occurs for modes with a wavenumber greater than about $k > 1/L$. A more rigorously derived and frequently encountered solution to this problem is [Haan June 1991, Hoffman 1994]

$$\gamma = \sqrt{\frac{gkA}{1+kL}},$$

which is not significantly different from Eq. (20).

Another important stabilizing effect in radiation ablated fluids comes from the ablation process itself. Think of the interface from the accelerating reference frame in which the heavy fluid is stationary, see Figure 2-2. Assume the perturbation in the heavy fluid has the classical fall off and growth rate, e^{-kz} and $e^{\gamma t}$, respectively. Consider the situation after a time, Δt from time zero. The perturbation has grown by $e^{\gamma \Delta t}$, but the interface has moved much deeper into the heavy fluid from ablation. The portion of the interface "shaved off" by ablation is given by $v_A \Delta t$, where v_A is the interface velocity in the heavy fluid. This is given by

$$v_A = \frac{1}{\rho_H}\frac{\partial m}{\partial t} = \text{(mass ablation rate per cm}^2\text{)}/\rho_{\text{H.}}$$

This movement of the interface results in a decrease in the perturbation amplitude of kv_A. The net growth is then [Haan June 1991]

$$\gamma = \gamma_c - \beta k v_A. \tag{21}$$

where β is a constant that must be determined by experiment and/or computation. The *c* subscript on γ refers to the classical growth rate. Eq. (21) is a simple formula that has not been rigorously derived, but is used extensively in ICF research and first introduced by Takabe [Takabe]. As with the density gradient problem, there is no rigorous closed form solution to the eigenvalue problem of an ablated interface.

Consider the implications of the ablation process. If $\gamma_c \leq \beta k v_A$, then the total growth rate is zero or negative, which occurs at the threshold wavelength of $\lambda = (2\pi\beta^2 v_A^2)/(gA)$. Wavelengths shorter than this value will not grow

Figure 2-2: Ablative Stabilization

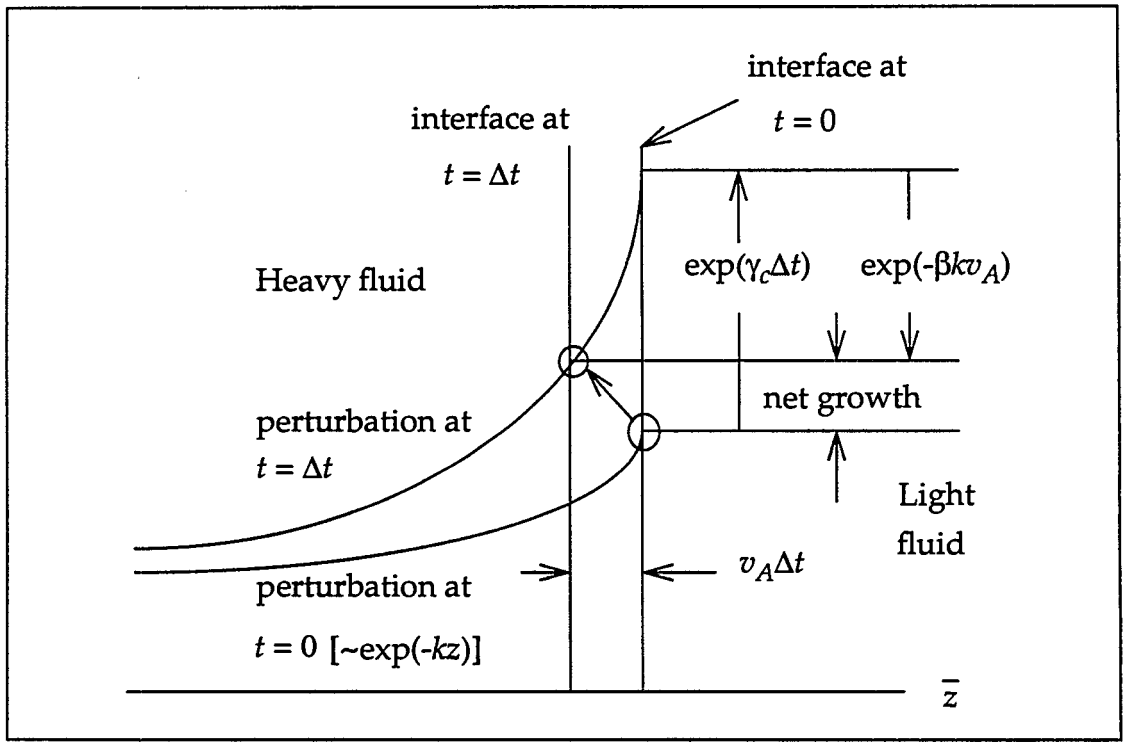

due to the stabilizing influence of the ablation. As the size of the wavelength is increased above this value, ablation will play less and less of an effect. Ablation, like the density gradient, serves to stabilize the shorter wavelengths.

One may combine the stabilizing effects of burn-off and a density gradient into one formula [Haan June 1991, Hoffman 1994]

$$\gamma = \sqrt{\frac{gkA}{1+kL}} - \beta k v_A. \tag{22}$$

Eq. (22) is an expression for incompressible fluids, while laser ablated plasmas are compressible. Compressibility effects produce a small net change in growth rate, under 20%, from the incompressible state depending on the size of the wavelength [Haan June 1991].

Some care should be taken with the application of Eq. (22). The linearized perturbation equations, Eqs. (10), assume the perturbed quantities to be small in relation to the equilibrium quantities. If this is not true, Eq. (22) is no longer valid. Eq. (22) is only applicable for small perturbations with an amplitude less than 10% of the wavelength, and early time periods in the growth.

A great deal of effort has been put into refining Eq. (22). However, there is some question as to the utility of continuing to refine the expression. Mathematical solutions require mathematical assumptions as to the nature of the density gradient, ablation rate, and many other properties of the system. The actual experimental values of these properties may not be well known. Eq. (22) is only as accurate as the assumptions which were used to create it. Refining the expression

to a mathematical level of accuracy beyond the uncertainties in the assumptions is futile.

2.2.3 Multiple Mode Rayleigh-Taylor Growth

At the onset of nonlinearity, the single mode begins to couple with itself, producing higher order harmonics which in turn couple with each other. The result of the addition of these higher order modes is the bubble and spike formation. The theory of mode coupling is important for a proper understanding of the Rayleigh-Taylor instability and the feed-out experiments. Both higher harmonics and bubble and spike formation were experimentally observed in some of the packages. One would expect that the growth of higher harmonics in the feed-out experiments would be slightly less than that predicted by the following theories. Both ablation and density gradients stabilize higher order modes more effectively than lower order ones, and both stabilization processes are present in the experiments.

Three models of the nonlinear Rayleigh-Taylor instability will be discussed, each corresponding to a different stage in its evolution. The first is Haan's weakly nonlinear mode coupling model which describes fluid behavior at the beginning of the nonlinear regime with only second harmonics present [Haan June 1991, August 1991]. A second Haan model assumes a later time, with many harmonics present and a large number of saturated modes. The last model by Youngs is applicable during late times the nonlinearity, when the interface is so

mixed that the concept of Fourier modes is no longer valid [Youngs].

In the early stages of the nonlinear regime, fundamental modes begin to couple with themselves creating second harmonics. Self-coupling is clearly seen in Haan's weakly nonlinear theory. The theory is a potential flow model and was derived assuming a plane interface between inviscid, incompressible fluids, with surface tension, T. The system is initially at rest in a gravitational field with the interface located at $z = \eta(\bar{x}, t)$, where $\bar{x} = (x, y)$. Periodic boundary conditions apply at the edges of a box of length L in the plane of the interface, and the fluid is assumed stationary as $z \to \pm\infty$. The interface may be decomposed into modes of a Fourier series. Their coefficients are given by

$$\eta_{\bar{k}}(t) = \frac{1}{L^2}\int \eta(\bar{x}, t) e^{-i\bar{k}\bullet\bar{x}} d\bar{x}, \tag{23}$$

where $\bar{k} = (k_x, k_y)$.

Let ϕ_H and ϕ_L be the velocity potentials in the heavy and light fluids respectively. These potentials may likewise be Fourier expanded in a consistent fashion with the boundary conditions

$$\begin{aligned} \phi_H(\bar{x}, z, t) &= \sum_{\bar{k}} \phi_{H\bar{k}}(t) e^{-kz} e^{-i\bar{k}\bullet\bar{x}} \\ \phi_L(\bar{x}, z, t) &= \sum_{\bar{k}} \phi_{L\bar{k}}(t) e^{-kz} e^{-i\bar{k}\bullet\bar{x}}. \end{aligned} \tag{24}$$

The pressure of each fluid is given by Bernouli's equation and is

$$p = \rho\left(\frac{\partial\phi}{\partial t} - \frac{v^2}{2} - gz\right). \tag{25}$$

There are three boundary conditions at the interface. First, the pressure step across the interface is determined by the surface tension and the curvature

$$\frac{\partial\eta}{\partial t} = \frac{\partial\eta\partial\phi}{\partial x\partial x}\bigg|_\eta + \frac{\partial\eta\partial\phi}{\partial y\partial y}\bigg|_\eta - \frac{\partial\phi}{\partial z}\bigg|_\eta. \tag{26}$$

This is actually two equations, ϕ may either be ϕ_H or ϕ_L. The two equations must agree, which is the second boundary condition. The third condition states that the pressure step across the interface must be a function of the surface tension and curvature of the interface

$$p_H - p_L = T\left(\frac{d^2\eta}{dx^2} + \frac{d^2\eta}{dy^2}\right) + HOT. \tag{27}$$

HOT refers to higher order terms that are neglected in this analysis.

Haan substitutes Eqs. (23) - (25) into the boundary conditions Eqs. (26) and (27). The boundary conditions are applied at $z = \eta(x, t)$ instead of $z = 0$, because the interface is located at $z = \eta(x, t)$. For example, the term $\partial\phi/\partial z$ would be expanded as

$$\frac{\partial\phi}{\partial z}\bigg|_\eta = \frac{\partial\phi}{\partial z}\bigg|_{\eta=0} + \eta\left|\frac{d^2\phi}{dz^2}\right|_{\eta=0} + HOT.$$

Combining the boundary conditions, Haan arrived at a differential equation for the time evolution of the interface

$$\ddot{\eta}_{\bar{k}} = \gamma^2(k)\eta_k + Ak\sum_{\bar{k}_2}\left[\ddot{\eta}_{\bar{k}_2}\eta_{\bar{k}_3}(1-\hat{k}_2\bullet\hat{k}) + \dot{\eta}_{\bar{k}_2}\dot{\eta}_{\bar{k}_3}\left(\frac{1}{2}-\hat{k}_2\bullet\hat{k}-\frac{1}{2}\hat{k}_2\bullet\hat{k}_3\right)\right]. \quad (28)$$

with $\bar{k}_3 = \bar{k}-\bar{k}_2$. k, k_2, and k_3 are wavenumbers, or magnitudes of the vectors. The unit vectors are defined as:

$$\hat{k} = \bar{k}/k \qquad \hat{k}_2 = \bar{k}_2/k_2 \qquad \hat{k}_3 = \bar{k}_3/k_3$$

The growth rate is not the classical because of the inclusion of surface tension, and is expressed as

$$\gamma(k) = \sqrt{gkA - \frac{Tk^3}{(\rho_H-\rho_L)}}.$$

If the second order terms are neglected, the solution to Eq. (28) for an initially stationary fluid is the standard linear result, as derived in the previous section, and is given by

$$\eta_{\bar{k}}^{lin}(t) = \eta_{\bar{k}}(0)\cosh[\gamma(k)t]. \quad (29)$$

Even if an exact solution to Eq. (28) including second order terms could be derived, its validity would be questionable, as terms of third order and higher were neglected in its derivation. These terms are certainly as important as the second order terms when the system is fully nonlinear. As a result, Eq. (28) is only valid during the weakly nonlinear phase of perturbation growth. Haan solved the equation approximately by substituting Eq. (29) into the terms on the right hand side of Eq. (28), which simplifies the expression. The result is a bit lengthy, but for most practical ICF applications it may be approximated as

$$\eta_{\bar{k}}(t) = \eta_{\bar{k}}^{lin}(t) + Ak\sum_{\bar{k}_2}\eta_{\bar{k}_2}^{lin}(t)\eta_{\bar{k}_3}^{lin}(t)2G(\bar{k},\bar{k}_2). \tag{30}$$

where $G(\bar{k},\bar{k}_2)$ is given by

$$G(\bar{k},\bar{k}_2) = \frac{\frac{1}{2}\gamma^2(k_2)[1-\hat{k}_2\bullet\hat{k}]+\frac{1}{2}\gamma(k_2)\gamma(k_3)\left[\frac{1}{2}-\frac{1}{2}\hat{k}_2\bullet\hat{k}_3-\hat{k}_2\bullet\hat{k}\right]}{\{[\gamma(k_2)+\gamma(k_3)]^2-\gamma^2(k)\}}.$$

Notice how the time and spatial dependence are neatly separated in Eq. (30). The origin of second harmonics is clearly seen in the second order coupling terms of the expression. A condition of applicability of Eq. (30) is that the modes contributing to the summation be adequately modeled by Eq. (29) because Eq. (29) was used to approximate these modes to obtain a solution. The fundamental modes must remain unchanged to second order for the theory to remain valid.

Mode coupling has a significant effect on perturbation growth from the Rayleigh-Taylor instability. Figure 2-3 shows this by applying Haan's model to three different cases of the Rayleigh-Taylor instability: single mode classical, multiple mode classical, and multiple mode stabilized by ablation and a density scale length. The solid lines in the Figure 2-3 represent the growth of an initial perturbation due to linear theory only, whereas the dashed lines show mode coupling results. The significance of the line delineating $1/k^2$ is the boundary between linearity and nonlinearity. As the modes of the spectrum reach this line, they grow more slowly, so there is a gradual progression of the fastest growing mode from high to low order. The fastest growing mode will be the smallest wavelength not

effectively stabilized or saturated. Thus small structures initially dominate the flow, evolving to larger and larger structures as the dominant wavelength increases.

Figure 2-3 shows mode coupling has a stronger influence on the classical than the ablative Rayleigh-Taylor instability because the fastest growing mode is much smaller in the classical than in the ablative instability. The smaller modes have a shorter e-folding time and form harmonics of both higher and lower frequencies quicker.

For evolution past the weakly nonlinear stage, Haan proposed a second model in which modes do not saturate based on their individual amplitude, but rather on the combined amplitude of modes within some distance ε from them in wavenumber space. After some analysis, the saturation amplitude was found to be

$$\eta_S(k) = \nu/(Lk^2).$$

where ν is a parameter taking into account ε and the amplitude at which the individual modes would saturate. Before a mode saturates, it grows linearly. After saturation, it will continue to grow at a constant rate equal to the linear rate at the time of saturation. This rate is

$$\eta_{Sat}(k, t) = \eta_S(k)\left[1 + \ln\frac{\eta_{lin}(k, t)}{\eta_S(k)}\right].$$

Figure 2-3: Mode Coupling

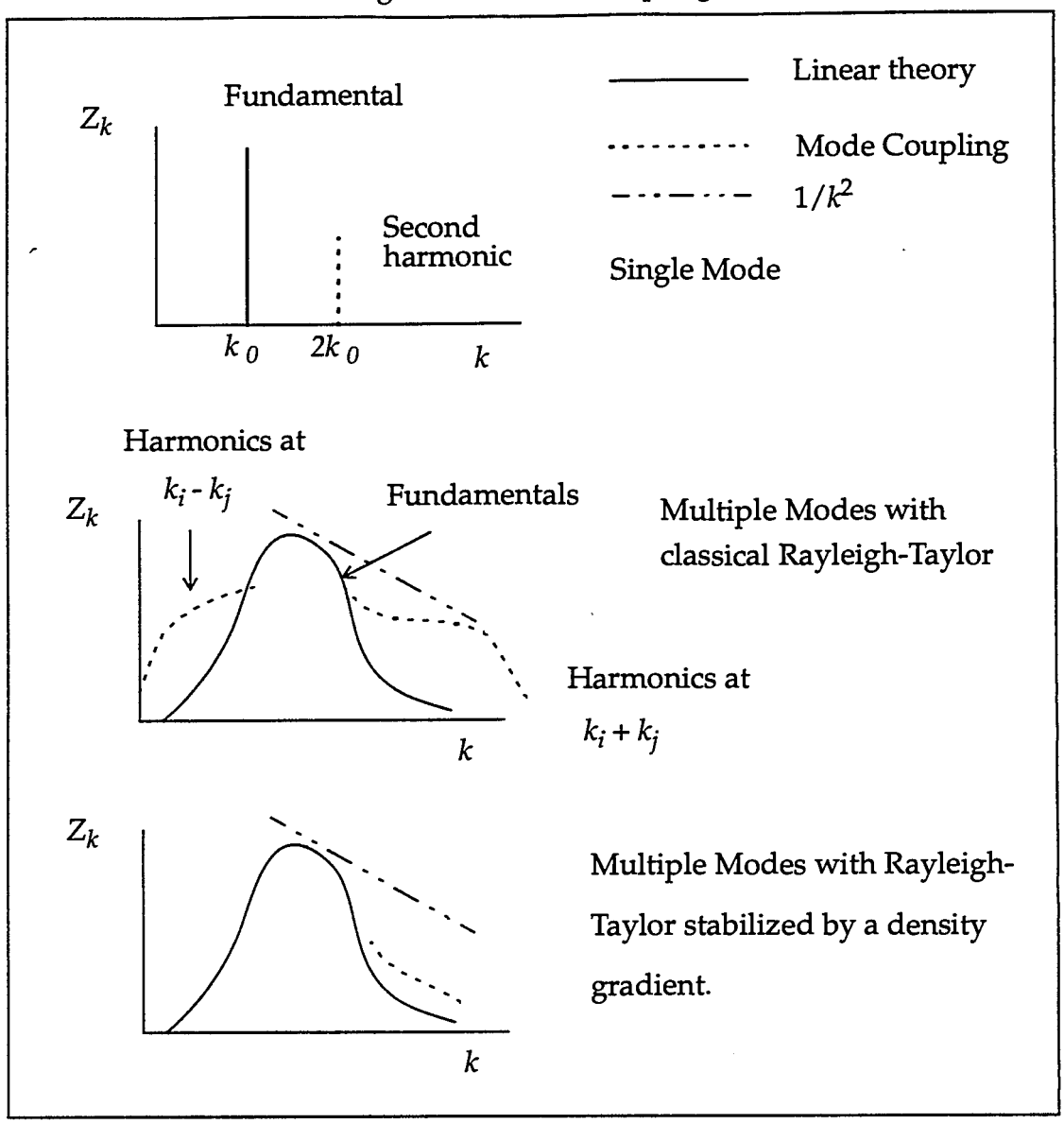

This theory is satisfactory for the ablative Rayleigh-Taylor instability, for which saturation is the most significant nonlinear aspect of the physics. It is thus useful for modeling most ICF plasmas. It is not applicable for classical Rayleigh-Taylor instability problems, as it does not include mode coupling which is the most important nonlinear effect in the classical Rayleigh-Taylor instability.

Ofer proposed a model combining Haan's mode coupling and saturation theories, which is applicable to both the classical and ablative Rayleigh-Taylor instabilities [Ofer].

After many modes have coupled and saturated, the interface reaches a disordered state where the two fluids mix. Bubbles and spikes have formed and Fourier modes are no longer a valid concept. Youngs computationally investigated the interpenetration of the fluids during this time. He found that the dominant wavelength continued to increase in size, as in the mode-coupling regime. The mechanism may be best understood through bubble competition rather than mode coupling. If a bubble of the lighter fluid is slightly larger than its neighbors, it grows more rapidly and eventually crowds out the surrounding bubbles. When the dominant wavelength reaches about ten times the wavelength of the initially fastest growing mode, the initial system parameters have been forgotten. The evolution could thus be predicted in all cases by simple expressions and no knowledge of original conditions.

A good measure of the evolution of the instability is the width of the mixed region, δ. For a given density ratio, the mixing process is described by a similarity solution with scale length proportional to gt^2 and may be expressed as

$$\delta = F\left(\frac{\rho_1}{\rho_2}\right) gt^2 . \tag{31}$$

If large amplitude, long wavelength perturbations are present, then the growth of the mixed region will exceed Eq. (31). To define δ, a volume fraction of the dense

fluid at the point (x, y, z) is used and designated $f_1(x, y, z)$. Let the initial interface between the fluids be in the x-y plane, with the z axis normal to the interface. The average of f_1 at a height z is then given by

$$\hat{f}_1(z) = \frac{\iint f_1(x, y, z)(dx)dy}{\iint (dx)dy}.$$

Integration over $dx\ dy$ refers to integration over the x-y plane. Youngs continued to define the following:

h_1 = the difference in height between the position the undisturbed interface would have reached and the point where $\hat{f}_1 = 0.99$, or the penetration of the light fluid.

h_2 = the difference in height between the position the undisturbed interface would have reached and the point where $\hat{f}_1 = 0.01$.

Then one has $\delta = h_1 + h_2$. Computational study and application of Eq. (31) showed

$$h_1 = \alpha \frac{(\rho_1 - \rho_2)}{(\rho_1 + \rho_2)} g t^2, \tag{32}$$

where $\alpha \cong 0.04 - 0.05$. Eq. (32) was confirmed experimentally, with values of α slightly higher than those derived computationally. Youngs found that the ratio h_2/h_1 increased as the density ratio increased. For the particular multimode calculations he performed he found

$$\frac{\rho_1}{\rho_2} = 3 \qquad \frac{h_2}{h_1} = 1.5$$

$$\frac{\rho_1}{\rho_2} = 20 \qquad \frac{h_2}{h_1} = 2.5$$

2.2.4 The Rayleigh-Taylor Instability in Stratified Fluids

Due to interface coupling, the growth of perturbations, whether from the Rayleigh-Taylor or Richtmyer-Meshkov instability, is different when the fluid is of a thickness on the order of a wavelength. The previous discussions relating to linear and multiple mode growth assumed an interface between two semi-infinite layers, where finite thickness effects were not a concern. Finite thickness effects are important in the feed-out packages, as the wavelength is 50 μm and the packages are from 35-86 μm thick. In addition, some of the packages contained a layer of beryllium on the cold side. As the initial densities of beryllium and aluminum are 1.8 and 2.7 g/cm^3 respectively, this resulted in three fluid interfaces where perturbations grew and interacted: the ablated material/aluminum, the aluminum/beryllium, and the beryllium/air interfaces. Because the fluids were compressible, these interfaces were not clearly distinct, but they formed density gradients as one fluid flowed into another. The incompressible theories presented here by Mikaelian and Ott provide insight into the compressible case.

One can clearly see the physics of interface coupling in Mikaelian's incompressible, linear model for stratified fluids [Mikaelian 1982, 1983, and 1995]. For example, take the situation where the densities on either side of a central

material are the same, giving the density pattern $\rho_A/\rho_B/\rho_A$. In this case, Mikaelian found that

$$\begin{aligned}
\eta_1(t) &= \frac{1}{2}\tan[\vartheta]\left\{\left(\cot\left[\frac{\vartheta}{2}\right]\eta_1(0)+\eta_2(0)\right)\cos[\gamma t]\right. \\
&\quad \left.+\left(\eta_2(0)-\tan\left[\frac{\vartheta}{2}\right]\eta_1(0)\right)\cos[\gamma t]\right\} \\
\eta_2(t) &= \frac{1}{2}\tan[\vartheta]\left\{\left(\cot\left[\frac{\vartheta}{2}\right]\eta_2(0)+\eta_1(0)\right)\cos[\gamma t]\right. \\
&\quad \left.+\left(\eta_1(0)-\tan\left[\frac{\vartheta}{2}\right]\eta_1(0)\right)\cosh[\gamma t]\right\},
\end{aligned} \tag{33}$$

where η is the perturbation on each interface, with the acceleration vector, g, pointing from the second to the first interface; t is time, γ is the growth rate for the system and ϑ is a coupling angle, which are both defined by the following set of equations:

$$\begin{aligned}
\sin[\vartheta] &= \frac{2W(z_1)/W(z_2)}{1+(W(z_1)/W(z_2))^2} \qquad \frac{\gamma^2}{g} = \frac{k(R-1)}{\sqrt{1+R^2+2R\coth[k\tau]}} \\
\frac{W(z_1)}{W(z_2)} &= 1+S\tanh\left[\frac{k\tau}{2}\right]+\frac{S}{R}\left(1+\sqrt{1+R^2+2R\coth[k\tau]}\right) \\
S &= \sinh[k\tau] \qquad R=\frac{\rho_B}{\rho_A}.
\end{aligned} \tag{34}$$

W may be thought of as the z spatial component of the $V_{\pi z}$ term in section 2.2.2. The z coordinate is perpendicular to the plane of the interface; τ is the thickness of the intermediate fluid layer. Interface coupling may be seen in Eq. (33). $\eta_1(t)$ is a function of both $\eta_1(0)$ and $\eta_2(0)$, as is $\eta_2(t)$. Even if η_1 was initially zero, it would

still grow due to the coupling. An interesting thing happens if one sets $\eta_1(0)/\eta_2(0) = \tan[\vartheta/2]$. The growing modes on both interfaces cancel, and the interfaces become stable. Likewise, if $\eta_1(0)/\eta_2(0) = \cot[\vartheta/2]$, the oscillatory modes cancel. This is a type of freeze-out, which is also seen in the Richtmyer-Meshkov interface coupling.

For the system of multiple interfaces, shown in Figure 2-4, the expression for the growth of an individual perturbation is somewhat more complex. A brief review of the derivation of this expression will now be presented.

Mikaelian's model assumes uniform density in each layer and neglects viscosity, surface tension, and heat transfer. The derivation starts with Eq. (17). For this derivation, one may replace $V_{\pi z}$ with just the spatial component in z, which will be designated here as W. The other two spatial components and time dependence may be canceled out of the equation. To obtain the jump condition,

Figure 2-4: Stratified Fluid Layers.

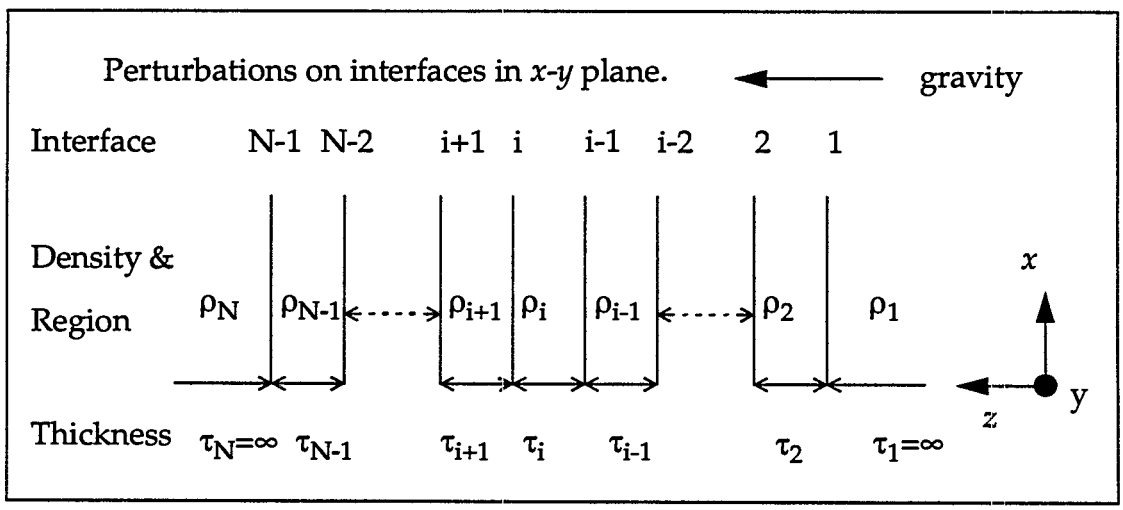

one again integrates Eq. (17) over each interface, but the result for the stratified fluids case is slightly altered from Eq. (18). It is given by

$$\Delta\left(\rho\frac{\partial W}{\partial z}\right)+\frac{gk^2}{\gamma^2}W\Delta(\rho)\;=\;0\,, \tag{35}$$

where the Δ operator refers to the difference in the fluid quantities above and below the interface. Eqs. (35) is a system of equations for N - 1 interfaces and may be written out as:

$$\begin{aligned}
B_1(W(z_1))+C_1W(z_2) &= \left(\frac{1}{\chi}\right)W(z_1) && i\;=\;1\\
A_iW(z_{i-1})+B_iW(z_i)+C_iW(z_{i+1}) &= \left(\frac{1}{\chi}\right)W(z_i) &&\\
A_{N-1}W(z_{N-2})+B_{N-1}W(z_{N-1}) &= \left(\frac{1}{\chi}\right)W(z_{N-1}) && i=N-1\,.
\end{aligned} \tag{36}$$

The subscripts on z refer to the value of z at the ith interface. The quantities in Eq (36) are defined as:

$$\begin{aligned}
A_i &= \frac{-\rho_i}{\sinh[k\tau_i](\rho_{i+1}-\rho_i)} \qquad C_i = \frac{-\rho_{i+1}}{\sinh[k\tau_{i+1}](\rho_{i+1}-\rho_i)} \qquad \chi=\frac{\gamma^2}{gk}\\
B_i &= \frac{\rho_{i+1}\Gamma_{i+1}+\rho_i\Gamma_i}{(\rho_{i+1}-\rho_i)} \qquad \Gamma_i = \left\{\begin{array}{ll}\tanh\left[\dfrac{k\tau_i}{2}\right]+\dfrac{1}{\sinh[k\tau_i]} & i\;=\;2\ldots N-2\\ 1 & i\;=\;1,N-1\end{array}\right\}.
\end{aligned} \tag{37}$$

This is an eigenvalue problem with eigenvalues $1/\chi$ and eigenvectors, W, and may be written in matrix form

$$MW = \left(\frac{1}{\chi}\right)W.$$

The matrix M is a $(N-1)$ X $(N-1)$ band matrix with elements A_i, B_i, C_i, from Eq. (36); W is an $N-1$ dimensional eigencolumn with elements $W(z_1), W(z_2), \ldots W(z_{N-1})$ which are the values of W at the interfaces. There are $N-1$ eigenvalues, each with its corresponding eigenvector. Unlike the single interface case, the eigenvectors do not correspond to the growth of a particular interface. The eigenvectors with their respective eigencolumns are referred to as normal modes. To obtain the growth at an individual interface, the contribution of all the normal modes to that interface must be summed. The relationship between W and η is simply, $W(z) = \partial\eta/\partial t$. Using this and summing over all modes one finds the amplitude at interface i to be

$$\eta_i(t) = \sum_{l=1}^{N-1}\sum_{j=1}^{N-1}\frac{W_l(z_i)}{W_j(z_l)}\left(\eta_j(0)\cosh[\gamma_l t] + \frac{\dot{\eta}_j(0)}{\gamma_l}\sinh[\gamma_l \tau]\right). \qquad (38)$$

The l subscript on W and γ relates each eigenvector to its respective eigenvalue. The γ used here is the one given in Eq. (37).

Mikaelian's theory is only valid in the linear regime, but Ott derived a theory for stratified fluids that is valid into the early stages of the nonlinear regime [Ott]. Unfortunately, the theory is limited in applicability to large Atwood numbers and large λ/τ, but may be used to provide insight into the evolution of the feed-out foils after the foils have become thin from ablation. The theory predicts the growth of perturbations on an infinitesimally thin ribbon of fluid sand-

wiched between massless fluids on either side. The derivation is elegantly simple. Using Newton's second law, Ott wrote an expression for the force on a differential length of the thin film, which included pressure and gravity. From the acceleration, he derived equations for the position as a function of time, which were a set of linear coupled partial differential equations. Solving these, he found the position of a piece of the thin film, originally located at $(x = \xi, y = 0)$ was given by

$$\begin{aligned} \bar{r}(x, y, t) &= x(\xi_0, t)\hat{x} + y(\xi_0, t)\hat{y} \\ x(\xi_0, t) &= \xi_0 - \sum_{K,\sigma} \xi_x^\sigma(K, t)\cos(K\xi_0 + \vartheta_K^\sigma) \\ y(\xi_0, t) &= \sum_{K,\sigma} \xi_y^\sigma(K, t)\sin(K\xi_0 + \vartheta_K^\sigma), \end{aligned} \tag{39}$$

where the functions $\xi_x^\sigma(K, t)$ and $\xi_y^\sigma(K, t)$ are solutions to

$$\ddot{\xi} + Kg\xi = 0. \tag{40}$$

The superscript σ, labels the four linearly independent solutions of Eq. (40). If one assumes $\xi \sim e^{-i\omega t}$, then there are two oscillatory roots with $\omega = \pm\sqrt{Kg}$, one growing root, $\omega = i\sqrt{Kg}$, and one decaying root, $\omega = -i\sqrt{Kg}$. As the K components do not correspond to a perturbation that is sinusoidal in space, the theory is nonlinear. Because of this, K and ω are similar to k and γ of the linear theory, but not identical.

Ott observed the evolution of a special case of Eqs. (39), with

$$\frac{g\partial\rho}{\rho\partial z} - \frac{g^2}{c_S} \geq 0,$$

where c_S is the sound speed. Stability is assured in a compressible system by a lack of density inversions on the interfaces. The maximum growth rate for any multilayer system with no surface tension, a free lower boundary and either a fixed or free upper boundary, is $\gamma = \sqrt{|g|/k}$.

Considering the multimode work of Haan in the light of the stratified fluid work presented in this section, one may realize that any harmonic modes generated by nonlinearity should couple across the interfaces. Interface coupling of the harmonics could result in the system approaching nonlinearity faster, as there would be additional second order terms in Haan's mode coupling expression. Such a coupling was not experimentally observed in the feed-out experiments, probably because the ablative stabilization discouraged harmonic growth on the hot surface.

2.2.5 The Richtmyer-Meshkov Instability

If a shock passes through a perturbed interface, the perturbation will usually grow. This is the Richtmyer-Meshkov instability. The effect of the shock is to briefly accelerate the perturbation, giving it a velocity with which it coasts afterward. This instability occurs in the feed-out packages when a shock created by hohlraum radiation interacts with a perturbation on the cold surface of the foil.

The growth of a perturbation under the influence of the Richtmyer-

$$x = \xi_0 - H\exp(t\sqrt{Kg})\cos\xi_0$$
$$y = H\exp(t\sqrt{Kg})\sin K\xi_0, \tag{41}$$

where the initial amplitude is given by H. This curve is composed of a number of sinusoidal modes, but as H becomes small, they all disappear except the fundamental $\sin K\xi_0$, and the solution approaches linear theory. Eq. (41) evolves into bubbles and spikes, with fluid flowing into the spikes from the bubbles on either side. When the ribbon of fluid folded back on itself forming a loop, the solution became unphysical. Mikaelian showed his linear theory to be equivalent to Ott's for cases of small perturbations [Mikaelian 1996].

Compressibility effects in stratified fluids are important for a more accurate understanding of the real systems encountered in experiment. Yang and Zhang theoretically studied general properties of stratified incompressible and compressible fluids using the linearized Euler equations [Yang 1993]. Their work provides some insights into compressibility effects in such systems. They proved that all eigenvalues, or perturbation growth rates, for a stratified fluid system are real and nondegenerate. They showed that a system of compressible fluids is always more unstable than an incompressible system with the same equilibrium density distribution. Two necessary and sufficient conditions for stability of a compressible system are for there to be no density inversions on any interface, and for

Meshkov instability may be estimated by applying the linear Rayleigh-Taylor instability model to the perturbation during the acceleration period of the shock. The perturbation will then grow according to

$$\eta(t) = \eta_0 e^{\gamma t}.$$

Take the second derivative of this expression with respect to time, then make the assumption that the time period during which the acceleration is nonzero is very small, such that $t \cong 0$ during this period. Then the exponential goes to one and we have the expression

$$\frac{d^2\eta}{dt^2} = \eta_0 g k A.$$

Integrating twice gives the perturbation amplitude as a function of time

$$\frac{\eta(t)}{\eta_0} = 1 + kAv_s t,$$

where v_s is the difference in fluid velocity across the shock. This simple analysis of the Richtmyer-Meshkov instability is referred to as the impulsive model and was first presented by Richtmyer [Richtmyer]. There are some difficulties with the impulsive model. It is only valid in the linear regime. The impulsive model also predicts immediate growth of the perturbation after shock passage. Of course this does not happen because the velocity imparted to the trough and crest of the perturbation are equal. Also, the shock compresses the perturbation and both fluids as it passes by. The amplitudes before and after shock passage are thus different, leading to some ambiguity in the expression.

Yang, Zhang, and Sharp compared the impulsive model to computational solutions of the linearized hydrodynamic equations, which are more accurate [Yang 1994]. They found the best agreement by using post-shock amplitudes for the reflected shock case and the average of the post- and pre-shock amplitudes for the reflected rarefaction. For the weak shock limit, the impulsive model and linear theory provide the same solution, but they diverge as shock strength increases. The agreement is also improved as the adiabatic exponents of the two fluids increase, while remaining approximately equal to one another. Good agreement was found to be particularly true for the reflected rarefaction case. The largest discrepancies occur when the adiabatic exponents are substantially different and the shock is very strong.

The impulsive model was presented here despite its flaws because it provides a clear insight into Richtmyer-Meshkov instability physics. For a more rigorous treatment of the instability, one may apply linear perturbation theory directly to the Richtmyer-Meshkov problem. First, a solution to the Riemann problem must be obtained, which is simply the problem of a shock hitting a flat interface. The hydrodynamic equations are then linearized around the solution to the Riemann problem. This two step process is necessary because the differential form of the hydrodynamic equations is not valid at the jump interface created by a shock, but only in the fluid on either side of a shock.

There is no closed form analytic solution to the Riemann problem, but there is a way to solve it geometrically by constructing a wave diagram in the

pressure-velocity plane, p-v plane, see Figure 2-5 [Yang 1994]. One can show for a given state of the fluid ahead of a shock, the velocity behind the shock is given by

$$v = v_a - (p - p_a)\left(\frac{\rho_a}{2}\right)^{-\frac{1}{2}}[(\gamma_G + 1)p + (\gamma_G - 1)p_a]^{-\frac{1}{2}}. \quad (42)$$

Figure 2-5: Riemann Problem

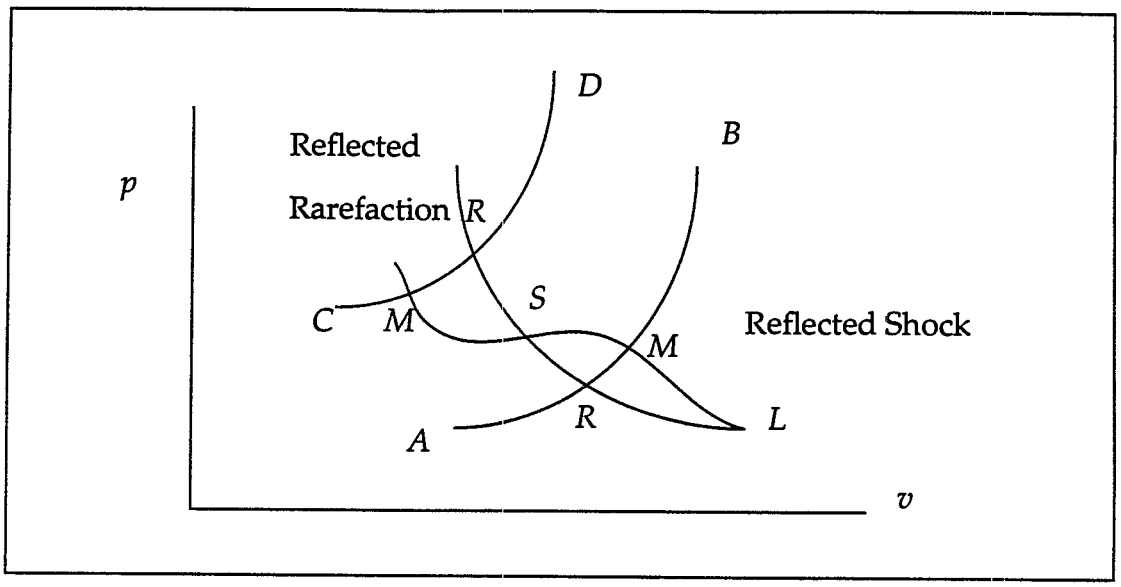

The subscripts a refer to the state ahead of the shock, whereas quantities without subscripts represent those behind the shock; γ_G is the adiabatic exponent of the gas. Eq. (42) is a curve in the p-v plane. Now consider what happens when a shock hits a discontinuity. There will be a transmitted shock, and either a reflected rarefaction or shock. Both the reflected and transmitted waves will have curves given by Eq. (42) on the p-v diagram. Curve ML is the curve for the transmitted shock, RL is for the incident shock, and AB is the reflected wave. The states of the fluid behind the transmitted shock and reflected wave must be the same. Thus,

the solution to the Riemann problem for the state of the material at the interface is the intersection of the two curves on the diagram, at point *M*. If point *M* is above *R*, as in the case shown for the curve *AB*, then the reflected wave is a shock. If *M* was below *R* on *AB*, a rarefaction would be the result.

Sometimes curves *ML* and *RL* cross at a point *S*, as shown in the figure. In such a case, as shock strength increases, *AB* moves upward to the position *CD*. On *CD*, *M* is below *R*, meaning the reflected wave is a rarefaction. Thus, whether a shock or rarefaction is reflected depends on the strength of the incident shock.

The nature of the reflected wave may be determined as follows. In general, if the incident shock moves from low to high impedance, $\gamma_{G2}\rho_2 \rightarrow \gamma_{G1}\rho_1$, then *M* is above *R* and a shock is reflected. From high to low, a rarefaction results and is referred to as "normal reflection." If the material properties of the two gases satisfy inequality (43)

$$\begin{aligned} \gamma_{G1} < \gamma_{G2} \rightarrow \quad & \frac{\gamma_{G1}}{\gamma_{G2}} \leq \frac{\rho_2}{\rho_1} \leq \frac{\gamma_{G1}+1}{\gamma_{G2}+1} \\ \gamma_{G1} < \gamma_{G2} \rightarrow \quad & \frac{\gamma_{G1}+1}{\gamma_{G2}+1} \leq \frac{\rho_2}{\rho_1} \leq \frac{\gamma_{G1}}{\gamma_{G2}}, \end{aligned} \tag{43}$$

then the situation is more complex, and curves RL and ML cross at the critical shock strength of

$$S = \frac{2(\gamma_{G1}\rho_1 - \gamma_{G1}\rho_1)}{(\gamma_{G1}-1)\rho_1 - (\gamma_{G2}-1)\rho_2} = \frac{p - p_a}{p}.$$

The subscripts 2 and 1 refer to the material the shock is moving from and into respectively. If *AB* is below point *S*, normal reflection occurs, but if it is

above, then normal reflection is reversed. If the shock strength is precisely S, then the impedances of the gases exactly match, and there is no reflected wave in linear analysis.

If there is an initial perturbation at the interface, then the shock or rarefaction reflected from the interface will also carry a perturbation. The reflected shock or rarefaction is the leading edge of the flow field of the Richtmyer-Meshkov instability. Fluid in the flow field will be imprinted with the perturbation. A perturbation on a shock will decay with time and distance away from the interface, but a perturbation on a rarefaction will neither grow nor decay. A stable perturbation on a rarefaction implies that the imprint on the ablation surface could be larger when the reflected wave is a rarefaction than a shock. The reflected wave in all the feed-out experiments was a rarefaction.

The perturbations at the interface may undergo one of two types of phase inversion: direct and indirect. Direct phase inversion is caused directly by the shock-interface interaction, and phase inversion occurs at or before the shock has passed the interface. In indirect phase inversion, the perturbations are not phase-inverted immediately after the shock has passed, but are moving in the direction of inversion. Later in the evolution of the interface, they invert. Direct inversion cannot occur when the reflected wave is a shock and only occurs when the reflected rarefaction is sufficiently strong. Indirect inversion rarely if ever occurs when the reflected wave is a shock. Thus, for a direct phase inversion to occur, the reflected wave must be a rarefaction.

Freeze-out is a condition where the perturbations neither grow nor decay after shock passage. This type of freeze-out should not be confused with freeze-out from interface coupling. No perturbation growth occurs because the shock reflected from the interface exactly cancels the effects of the shock transmitted through the interface. This situation can occur for both reflected rarefactions and shocks, but it cannot occur if the two adiabatic exponents are equal. It is believed impossible for freeze-out and total transmission to occur at the same time.

Just as the impulsive model is not as rigorous as the linear model, the linear equations are not as accurate as the nonlinear hydrodynamic equations. Each model predicts a different growth rate with time. To study the differences between these models, Holmes, Grove and Sharp computationally investigated the Richtmyer-Meshkov instability between air and SF_6, and between air and He [Holmes]. They compared the results of the linear model to nonlinear hydrodynamic equations. The shock strength was Mach 1.2 in air, and the perturbations 0.24 cm in amplitude and 3.75 cm in wavelength. A sketch of their general results is shown in Figure 2-6. Twice there were deviations of the linear from the nonlinear results at 70 and 200 μs. Both of these deviations result in a decrease in the growth rate from the linear prediction and are generated by the creation of secondary shocks from nonlinear interactions. The secondary shock interaction at 200 μs is so strong, it results in a permanent deceleration of the bubble. In addition, the linear solution contains acoustic waves, whereas in the nonlinear case

Figure 2-6: Typical Richtmyer-Meshkov Growth Rate

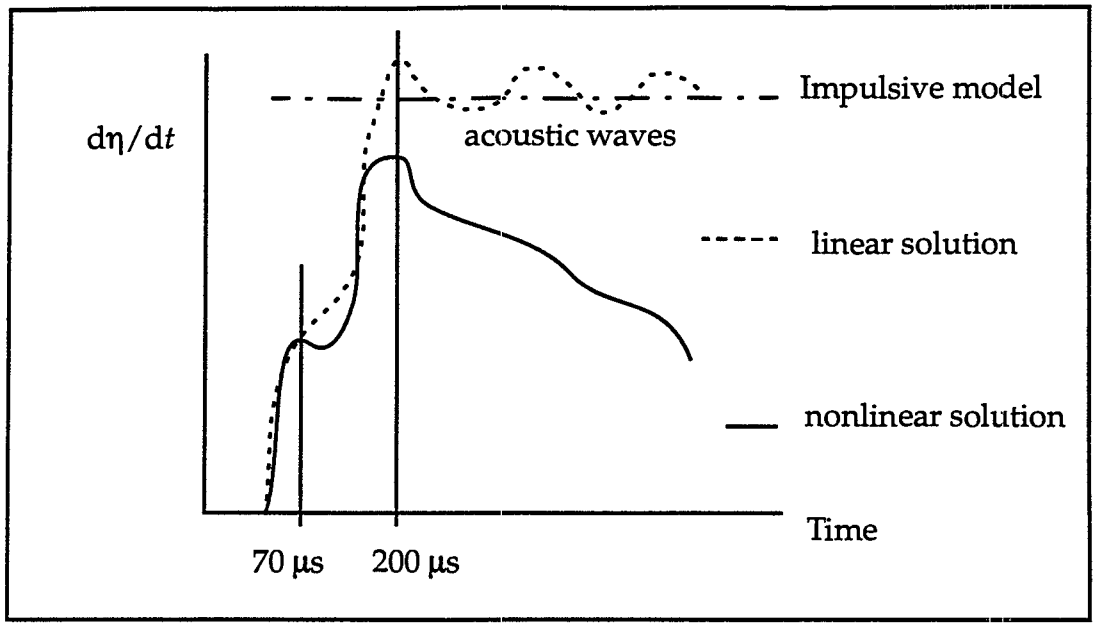

these waves may steepen into secondary shocks. There are two important features of the linear solution causing these differences. Characteristics are not allowed to focus, creating secondary shocks, and linearization constrains the geometry of the wave fronts to be sinusoidal.

As with the Rayleigh-Taylor instability, mode coupling occurs in the Richtmyer-Meshkov instability. Mode coupling is slower in a Richtmyer-Meshkov instability because the fluid is under acceleration for a much shorter time than in the Rayleigh-Taylor instability. Given sufficient time, the harmonics combine to form bubbles and spikes. Haan extended his mode coupling model for the Rayleigh-Taylor instability to the Richtmyer-Meshkov instability [Haan August 1991]. The impulsive model was used, with the assumption that $g = 0$ and the perturbation is coasting at some constant velocity, which leaves the derivation of Eq.

(28) unchanged. The solution is

$$\eta_{\bar{k}}(t) = \eta_{\bar{k}}^{lin}(t) + \frac{1}{2}Ak\sum_{\bar{k}_2}\eta_{\bar{k}_2}^{lin}(t)\eta_{\bar{k}_3}^{lin}(t)\left[\frac{1}{2} - \hat{k}_2 \bullet \hat{k} - \frac{1}{2}\hat{k}_2 \bullet \hat{k}_3\right],$$

assuming the dominant modes have been growing long enough that

$$\eta_{\bar{k}}^{lin}(t) \gg \eta_{\bar{k}}^{lin}(0).$$

During late times, the bubble and spike velocities may be described by the power law, $v = ct^{-\alpha}$ where c and α are some constants [Holmes].There is a sharp contrast between these exponentially decaying velocities of the Richtmyer-Meshkov and Rayleigh-Taylor instabilities. In the Rayleigh-Taylor instability, the bubble approaches a constant velocity and the spike undergoes free fall for high Atwood numbers.

2.2.6 The Richtmyer-Meshkov Instability in Stratified Fluids

If there are multiple fluid interfaces within the distance of several perturbation wavelengths of each other, a Richtmyer-Meshkov instability on one will couple with all the other interfaces. The situation with multiple interfaces is shown in Figure 2-4, with the gravity vector pointing in the direction of acceleration from the shock. Even if an interface is stable by itself, coupling with the unstable interfaces will produce perturbation growth. This is analogous to the Rayleigh-Taylor interface coupling discussed in section 2.2.3. Richtmyer-Meshkov interface coupling is one of the two mechanisms by which the perturbation on the

cold surface of a radiation driven foil feeds-out to the ablation surface. It is thus important in understanding the feed-out experiments. The second mechanism, differential acceleration, will be discussed in section 2.2.7.

A theoretical basis is always a good start for the study of any phenomenon of interest. Mikaelian extended his stratified fluid theory to the Richtmyer-Meshkov instability using the impulsive model [Mikaelian 1985, 1995]. The result is a simple expression that clearly shows the physics of interface coupling but does not address such complexities as compression or radiation. Taking the second derivative of Eq. (38) and replacing g with $v_s\delta(t-t_s)$ where t_s is the shock arrival time, then integrating twice gives

$$\eta_i(t) = \eta_i(0) + \dot{\eta}_i(0)t + v_s \sum_{l=1}^{N-1} \sum_{j=1}^{N-1} \Gamma_l^2 \frac{W_l(z_i)}{W_j(z_l)} (\eta_j(0) + \dot{\eta}_j(0)t_s)(t-t_s)\Theta[t-t_s]. \quad (44)$$

There are some problems with this expression. It assumes the same velocity is imparted to each interface by the shock, which is unrealistic. As the shock interacts with each interface, either a reflected shock or rarefaction will result, which will interfere with the growth on other interfaces. Also, Eq. (44) assumes the velocity from the shock is imparted at the same time to all the interfaces, which is unrealistic. To apply Eq. (44), the acoustic impedances of the interfaces must match or be very close, and the time necessary for the shock to pass through the various layers must be short compared to the growth rates of the instabilities. Nevertheless, one may use Eq. (44) to learn about interface coupling of the Richtmyer-Meshkov instability.

By taking a two-interface problem where the densities on each side of the middle layer are the same in the pattern $A/B/A$, Eq. (44) simplifies considerably to

$$\begin{aligned} \eta_1(t) &= \eta_1(0) + \frac{v_s\Gamma^2}{\cos[\vartheta]}(\eta_1(0) - \sin[\vartheta]\eta_2(0))t \\ \eta_2(t) &= \eta_2(0) + \frac{v_s\Gamma^2}{\cos[\vartheta]}(\eta_2(0) - \sin[\vartheta]\eta_1(0))t, \end{aligned} \tag{45}$$

where ϑ is a coupling angle. ϑ is again defined by Eq. (34). Subscripts 1 and 2 refer respectively to the first and second interfaces the shock hits.

Eq. (45) has many interesting characteristics. Interface coupling and feedthrough can easily be observed here. In addition, if $\eta_1(0)/\eta_2(0) = \sin[\vartheta]$, then the first interface does not grow. Likewise, if $\eta_2(0)/\eta_1(0) = \sin[\vartheta]$, the second interface does not grow. The freeze-out described here for the Richtmyer-Meshkov instability is similar to freeze-out in Rayleigh-Taylor interface coupling, with the exception that only one of the two interfaces may be frozen at the same time. Freeze-out with the Richtmyer-Meshkov instability has been computationally observed but remains to be experimentally verified [Mikaelian 1996].

As an educational exercise, the growth rates of three cases, the second of which corresponds to the feed-out experiments, are considered using Eq. (45):

Case *A*: $\eta_1(0) = \eta_2(0) = \eta_0$ sinuous shape,

Case *B*: $\eta_1(0) = \eta_0 \qquad \eta_2(0) = 0$,

Case *C*: $\eta_1(0) = -\eta_2(0) = \eta_0$ varicose shape.

A density ratio of $\rho_B/\rho_A = 3$ is used and a normalized growth rate for the i^{th} interface is defined as, $NGR_i = \dot{\eta}_i/(\eta_0 v_s k)$. The normalized growth rate is the coupled growth rate divided by the growth rate of an uncoupled interface with an Atwood number of one. Because the fluid interfaces in this example do not have an Atwood number of one, the normalized growth rate is not exactly unity when the interfaces are growing classically. Figure 2-7 shows a sketch of approximately how this value varies with $k\tau$. For $k\tau = 10$, all of the interfaces have decoupled, and the classical growth rates are observed, but for $k\tau$=0.01, the interfaces have completely coupled, and have the same growth rates. Case *A* turns into a varicose shape after shock passage, as the interfaces grow in opposite directions. Freeze-out occurs in this case for low $k\tau$. Case *B* is representative of the situation in the feed-out experiments. As $k\tau$ becomes small in this case, interface 2 begins to grow with interface 1, even though it has no perturbation, producing a sinuous shape which was experimentally verified with face-on radiography. The growth rates actually increase over the classical value as the two interfaces couple. The growth rates in Case *C* are also larger than classical for strong interface coupling. Both interfaces always have the same growth rate in this case. Case *C* also becomes sinuous, but more strongly so than Case *B*. One can see that interface coupling can either increase or decrease the classical growth rate depending on the situation.

Figure 2-7: Sketch of Normalized Growth Rate

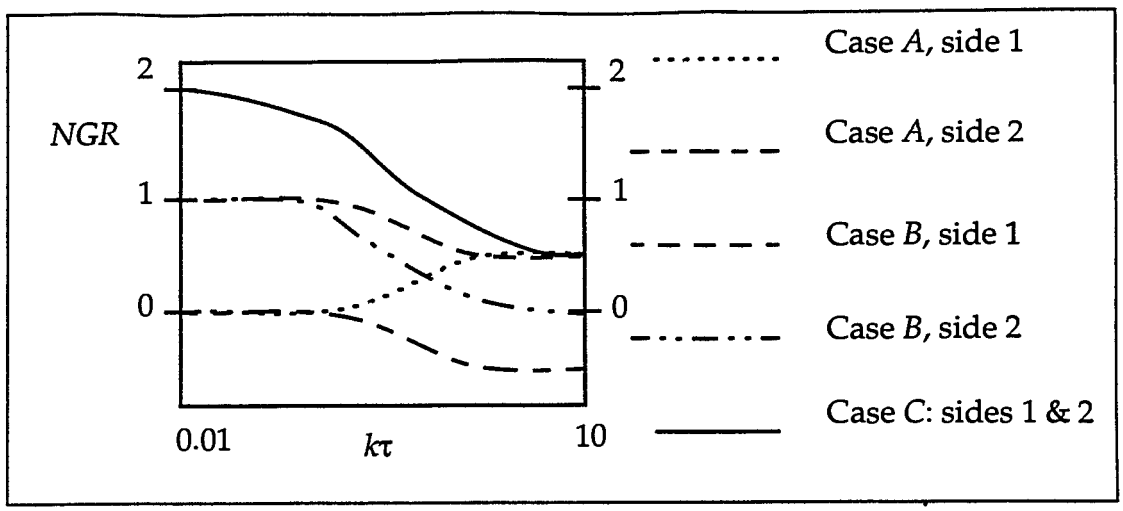

Nonlinearity, compressibility, and density gradient effects have significant influence on interface coupling with the Richtmyer-Meshkov instability but are not included in Mikaelian's theory. All three of these effects are present in the feed-out packages. Systems with these characteristics are too complex to be analyzed with theory, and are always either computationally or experimentally studied. A paper by Baltrusaitis presented calculations and experiments performed in order to study the Richtmyer-Meshkov instability in thin films that were nonlinear, compressible, and had a density gradient [Baltrusaitis]. SF_6 gas flowed through a contoured nozzle into a shock tube filled with air. Both sides of the nozzle were corrugated, producing a gas curtain with a varicose cross section and diffusive boundaries. The exact shape of the perturbations could not be controlled precisely from shot to shot, but the initial conditions were recorded before each shot. The dominant wavelength of the initial perturbation was about 6 mm, while the curtain thickness was around 3 mm. The shock was a Mach 1.2. Diffusion of

the gas formed a density gradient at the fluid interfaces, similar to the density gradient formed in the feed-out packages from preheat.

Three different types of flow pattern were observed and modeled. Upstream mushrooms developed when the initial perturbations were predominantly on the upstream side of the gas curtain, or when the amplitude of the upstream perturbation was much greater than the downstream perturbation. Likewise, downstream mushrooms evolved from a large perturbation on the downstream side of the curtain. A sinuous pattern developed with no mushrooms when both interfaces had roughly equal perturbation amplitudes, or the downstream side was slightly larger. The gas curtain remained intact between the mushrooms, connecting them in a bubble formation. Because SF_6 is heavier than air, the shock on the upstream side generated growth but no phase inversion. The shock created growth and phase inversion of the downstream perturbations. Thus, for an initially varicose curtain, the phase of the downstream side would be inverted to match the upstream, forming a sinusoidal pattern.

These results may be understood by considering vortex dynamics. As the pressure gradient from the shock interacts with the density gradient at the interfaces, it generates vorticity. The strength of this vorticity is directly proportional to the amplitude of the perturbations. Thus, the interface with the largest amplitude has the largest vorticity, and dominates the flow. Computational analysis showed that only one pair of vortices were in the gas curtain, the competing vortex pair from the weaker interface having been overcome by the larger. Even

in the sinuous case, where both amplitudes were equal, there was only one vortex, albeit a much weaker vortex than those of the mushroom curtains.These results may also be understood from an interface coupling standpoint. When the ratio of thickness to wavelength is small, Mikaelian's interface coupling theory predicts that the perturbation grows on the entire ribbon of fluid as a unit, not separately on the interfaces. This was certainly the case with the gas curtain experiments and is the reason for the gas curtain having to "select" one vortex pair to dominate its evolution. A very similar selection between the Rayleigh-Taylor and Richtmyer-Meshkov vortices was observed in the feed-out calculations and is described in chapter 5.

Mikaelian computationally modeled the experiments in the Baltrusaitis paper and predicted an additional flow pattern that was not observed in the experiments [Mikaelian 1996]. If the curtain was initially sinuous, Mikaelian predicted that both upstream and downstream mushrooms would develop. Perturbations are initially in phase in a sinuous pattern. The shock reversed the phase of the downstream perturbation creating a varicose pattern, which created double mushrooms as it continued to expand.

So far, Richtmyer-Meshkov and Rayleigh-Taylor interface coupling has been discussed as two separate issues, but the two are a coupled system in the feed-out process. The only publications found investigating such a coupled system were by Bel'kov [Bel'kov]. Calculations were performed on laser driven foils with an initial perturbation on the cold side, very similar to the packages

described in this dissertation. Foil thicknesses of 3 and 5 μm were selected, with perturbation wavelengths of 10 and 2 μm. Calculations were first run with these modes on the hot surface of the package, then on the cold surface to observe the difference in results. Both single and multiple modes were studied to observe mode coupling in feed-out. Ott's model agreed with the computational results very well, both for initial perturbations on the front as well as on the back. The applicability of Ott's theory indicates the foil was sufficiently thin compared to the wavelength that both interfaces were strongly coupled and grew at the same rate. Qualitatively, it was shown that the interaction of the two modes differed somewhat when the perturbations were placed on the hot or cold surfaces. The difference was caused by acoustic-gravity waves being generated in the case of perturbations on the cold surface, but not generated when the perturbations were initially on the ablation surface. Acoustic-gravity waves are part of the Richtmyer-Meshkov instability and are a subject discussed in the next section. Unlike the Bel'kov calculations, the feed-out foils move from states where the Richtmyer-Meshkov and Rayleigh-Taylor instabilities are not coupled to the state where there is complete coupling and the Rayleigh-Taylor instability dominates.

2.2.7 Atmospheric Type Modes

The calculations and experimental data both suggest that all the feed-out packages have an internal oscillatory mode which interacts with the instabilities. Because of the acceleration of the foils, there are at least three important inter-

nal modes allowed by the physics. These are the acoustic, gravity, and Lamb modes, which are all present in the atmosphere. After these three candidates had been identified the task was to determine which mode was present in the experiments. The acoustic mode is usually associated with the Richtmyer-Meshkov instability as sketched in Figure 2-6 so it was initially considered the most likely candidate. Indeed, later calculations indicated that the mode in the feed-out packages was probably acoustic; however, a short description of each is presented here because it is necessary to understand how to differentiate between the three modes. In addition, the physics of the packages allows for all three, and any one of them could be found in future experiments similar to the ones presented here.

The acoustic mode has a different dispersion relation than classical acoustic waves under the influence of acceleration. A general dispersion relation for the acoustic and gravity modes is presented in Gossard and Hooke [Gossard]

$$\left(\frac{N^2}{\omega^2}-1\right)\left(1-\frac{\omega^2}{k^2c_S^2}\right)=\frac{\Gamma^2}{k^2}. \tag{46}$$

The symbol N^2 is called the Väisälä-Brunt frequency and is given by

$$N^2=-g\left(\frac{1}{\rho}\frac{\partial\rho}{\partial z}+\frac{g}{c_S^2}\right),$$

while Γ is termed the Eckart coefficient,

$$\Gamma=\frac{1}{2\rho}\frac{\partial\rho}{\partial z}+\frac{g}{c_S^2}.$$

Eq. (46) was originally derived as the dispersion relation for internal oscillatory

modes propagating in the atmosphere and is for the special case of a nonrotating earth. The z coordinate is altitude. Because the density and sound speed are a function of altitude, the Eckart coefficient and Väisälä-Brunt frequency are also. The expression assumes no vertical component to the propagation.

The atmosphere is much like the feed-out foils and ICF packages in general. It is a compressible fluid, under the influence of a gravitational field, and decreases in density with altitude just as the ablation and cold surfaces of the foil decrease in density as one moves away from the center. There are four roots to Eq. (46) which are forward and backward propagating acoustic and gravity modes.

The gravity mode may be understood in terms of an internal Rayleigh-Taylor instability. In incompressible fluids, the Rayleigh-Taylor instability is a mode that oscillates as a stable wave if γ is imaginary, or, if γ is real, has growing and decaying parts. In either case, the Rayleigh-Taylor instability exists on the interface of the fluids and is driven by gravity. Any penetration into the fluids of a growing perturbation drops off exponentially from the interface. In a compressible fluid, the mode may exist inside the fluid itself in which case it is an internal gravity wave. To visualize this, imagine a fluid particle in a gas which has a variable density with height due to a gravitational field. If the fluid particle rises, its pressure will drop to equilibrate with the surrounding fluid, but it will still be slightly denser than the fluid at that height. As a result, it will be pulled by gravity back to equilibrium, and due to inertia, pass the equilibrium position, moving lower to a position of buoyancy. The oscillation may be stable, or increase in

amplitude with time depending on the fluid conditions.

An approximate sketch of the solutions to Eq. (46) is shown in Figure 2-8. The acoustic branch of Eq. (46) is given by the conditions $\omega^2/k^2 > c_S^2$ and $\omega > N$. It approaches the classical acoustic dispersion relation for large k,. For small k, it has a cutoff frequency, $N_A^2 = N^2 + c_S^2\Gamma^2$, below which it does not propagate. The gravity branch is given by the conditions $\omega^2/k^2 < c_S^2$ and $\omega < N$. It does not propagate above the Väisälä-Brunt frequency, which it asymptotically approaches as k becomes large. One may see that differences in the dispersion relations is the key to distinguishing between the acoustic and gravity modes. The Lamb mode is defined by the intermediate condition for a nonrotating earth, $\omega^2/k^2 = c_S^2$, which is just the classical acoustic dispersion relation. Because of this, the Lamb mode is not always easily distinguishable from the acoustic mode

Figure 2-8: Atmospheric Type Modes

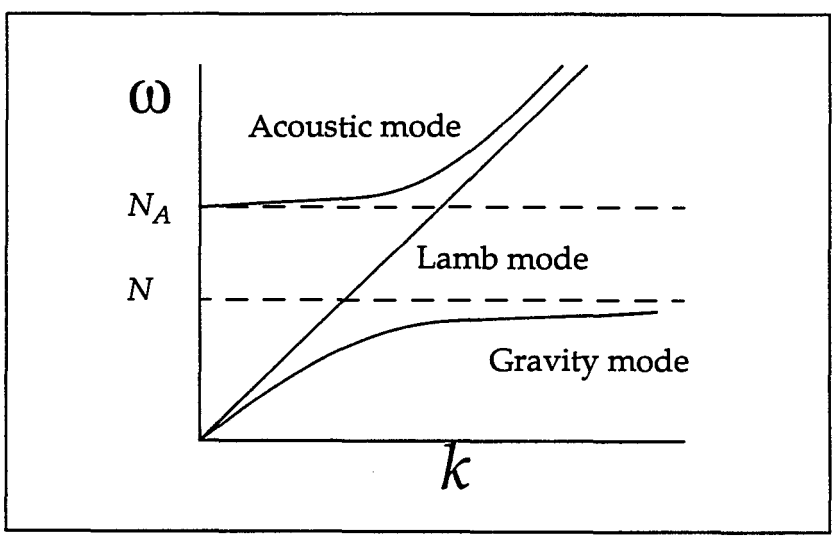

based on the dispersion relation alone.

Depending on the state of the fluid, the gravity and Lamb modes may have a real component, making them unstable. The first to investigate this in relation to inertial fusion plasmas was Scannapieco [Scannapieco]. He performed a linear perturbation analysis on the equations of hydrodynamics, similar to the one in section 2.2.2, with two important differences. He assumed a zeroth order density variation in the direction of gravity of, $\rho_0(z) = \rho_0(0)e^{z/H}$ where H is a scale length, and he assumed compressibility. The equivalent expression to Eq. (19) was no longer second-order, but rather an eighth-order polynomial in γ, admitting complex conjugate pairs of gravity, acoustic, and Lamb modes. As the value of H changed, so did the stability of the modes. Table 2-1 shows the stable and unstable modes. The symbol γ_G is the adiabatic gas constant. The acoustic modes are always oscillatory. The classical Rayleigh-Taylor instability is the growing internal gravity mode for $H > 0$, however, the growing gravity mode for $H > -c_s^2/g$ is not a Rayleigh-Taylor mode. The Lamb mode is the most interesting, as it has a real component to the growth rate for all but the specific case of $H = -c_s^2/\gamma_G g$. The Lamb mode is almost always unstable.

Table 2-1: Mode Stability

H	Acoustic	Gravity	Lamb
$H > 0$	oscillatory	growing	growing-oscillatory
$H > -c_s^2/\gamma_G g$	oscillatory	oscillatory	growing-oscillatory
$H = -c_s^2/\gamma_G g$	oscillatory	oscillatory	oscillatory
$H < -c_s^2/\gamma_G g$	oscillatory	oscillatory	growing-oscillatory
$H > -c_s^2/g$	oscillatory	growing	growing-oscillatory

Scannapieco's results have important ramifications for the feed-out foils and ICF capsules. They imply that internal fluid instabilities may exist in addition to the Rayleigh-Taylor and Richtmyer-Meshkov surface instabilities. The internal instabilities could be disruptive or benign to capsule performance. Scannapieco's paper indicated that Lamb instabilities would probably saturate rapidly after growth in the linear phase. Thus, to distinguish between acoustic and Lamb modes, one looks at the linear behavior. If there is growth and an acoustic-like dispersion relation, the mode is probably a Lamb mode.

2.2.8 Differential Acceleration

Feed-out of a perturbation from the cold to the ablation surface occurs by at least two mechanisms. Richtmyer-Meshkov interface coupling, which was described in section 2.2.6, is one mechanism, and differential acceleration is another. Both of these effects result in a perturbation on the ablation surface 180°

out of phase with the original perturbation on the cold surface. Both differential acceleration and interface coupling seed the Rayleigh-Taylor instability and growth on the ablation surface begins.

Differential acceleration may be understood by considering two columns of fluid, one running through the trough of the initial perturbation and the other running through the peak. The column of fluid running through the peak will have a greater mass. Because the force of ablation from the X-ray drive is uniform across the hot surface, the acceleration of the thinner column will be greater than that of the thicker one. As the thinner column begins to move past the thicker, a perturbation will appear on the hot surface.

A simple expression predicting the feed-out from differential acceleration is easily derived [Hoffman 1997], see Figure 2-9. The mean acceleration of the foil is $g = F/m$ where F is the ablative force and m the average foil mass. The mean position of the hot surface, $x(t)$, neglecting ablation, is $x(t) = gt^2/2$. The ratio of the difference in mass of the fluid columns, Δm, to the average mass may be written, $\Delta m/m = \eta_0/\tau$. Combining these three equations, the amplitude of the perturbation on the front surface is $\eta_{DA}(t) = \Delta x(t) = x(t)\eta_0/\tau$. Differentiating to obtain the growth rate, one finds, $\dot{\eta}_{DA}(t) = \dot{x}(t)\eta_0/\tau = v_{PS}\eta_0/\tau$, where v_{PS} is the post shock velocity of the fluid. The acoustic waves generated by the Richtmyer-Meshkov instability will cause the differential acceleration to saturate as the cold surface perturbation phase inverts. Saturation is expected to occur on a

time scale on the order of the frequency of the acoustic wave, which is approximately $t_{PI} = \lambda/c_S$. The maximum growth from differential acceleration is then $\eta_{DAmax} = (v_{PS}/c_S)(\lambda/\tau)\eta_0$. Note that this expression is a function of λ/τ, like interface coupling.

Figure 2-9: Differential Acceleration